

Experimental Validation of Provably Covert Communication Using Software-Defined Radio

Rohan Bali[✉], Trevor E. Bailey[✉], Michael S. Bullock[✉], and Boulat A. Bash[✉]

Abstract—The fundamental information-theoretic limits of covert, or low probability of detection/intercept (LPD/LPI), communication have been extensively studied for over a decade, resulting in the *square root law* (SRL): only $L\sqrt{n}$ covert bits can be reliably transmitted over time-bandwidth product n , for constant $L > 0$. Transmitting more either results in detection or decoding errors. The SRL imposes significant constraints on the hardware realization of mathematically guaranteed covert communication. These preclude the use of standard link maintenance operations that are taken for granted in non-covert communication. Thus, experimental validation of covert communication is underexplored: to date, only two experimental studies of SRL-based covert communication are available, both focusing on optical channels. Here, we demonstrate provably secure covert radio-frequency (RF) communication using software-defined radios (SDRs). We combine system design, theory, and experiments by 1) developing a sparse-signaling pulse shape to enable covert transmission of data in an environment with potential mobility, 2) proving the covertness of the resulting system, and 3) validating the theoretical predictions by implementing it on SDRs. We uncover and address unique challenges specific to using SDR architecture for covert communications. This opens practical avenues for implementing covert communication systems and raises further research questions.

Index Terms—Software radio, Information theory, Communication system security, Signal detection, Wireless communication

I. INTRODUCTION

Covert, or low probability of detection/intercept (LPD/LPI) communication, allows transmitting messages without alerting an adversary [1]–[4]. This mode of information security is highly desirable and contrasts with the traditional cryptographic [5] and information-theoretic secrecy [6] methods that prevent adversaries’ access to the transmission’s content, but not its detection. Careful waveform design and spread spectrum techniques are often employed in practice to reduce adversaries’ signal-to-noise ratio (SNR) below the noise floor [7, Pt. 1, Ch. 5]. However, mathematically guaranteeing covertness requires following the *square root law* (SRL): only $B(n) = L\sqrt{n}$ covert bits can be reliably transmitted over n channel uses [1]–[4]. The channel-dependent constant $L > 0$ is called *covert capacity* and $n = TW$ is typically the time-bandwidth product for the transmission. Notably, the Shannon capacity [8] of this channel is zero, since $\lim_{n \rightarrow \infty} \frac{B(n)}{n} = 0$. This is because the adversary’s task in covert communication involves learning just one bit of information (whether the

transmitter is on or not) versus $\mathcal{O}(n)$ bits of transmitted data in traditional secure communication. Nevertheless, a significant number of such mathematically guaranteed covert bits can still be transmitted within a finite time.

The discovery of the SRL in [1], [2] resulted in an explosion of research by the communication and information theory communities, as overviewed in a tutorial [3] and a detailed survey [4]. This included characterization of capacity L for additive white Gaussian noise (AWGN) and discrete memoryless channels (DMCs) [9]–[12], covert networks [13]–[25], quantum aspects of covert communication [26]–[37], covert communication with unmanned aerial vehicles (UAVs) [38]–[43], and many other directions outlined in recent surveys [4], [43], [44] and references therein.

An adversary lacking knowledge can improve covert communication. For example, an adversary’s uncertainty of transmission time/frequency yields a multiplicative enhancement to covert capacity L [45]–[47]. Uncertainty in adversarial channel noise power levels, from, e.g., jammer assistance, can, in theory, lead to a linear law: $\mathcal{O}(n)$ covert bits reliably transmissible over n channel uses [39], [48]–[51]. However, one must approach the assumptions underlying these results with care, e.g., if the underlying channel is continuous-time, transmissions that break the SRL are detectable [52].

On the contrary, the SRL arguably governs the worst case by assuming the adversary knows the transmitter-adversary channel’s characteristics, exact transmission time/frequency, and transceiver design. As detailed in Section II, the adversary’s only limitations are: 1) inability to control the random channel noise; and 2) lack of access to the secret shared between transmitter and receiver prior to the transmission. Therefore, the SRL, while conservative, provides a high level of security against unforeseen adversarial technological surprises. Unfortunately, the strict output power constraint of SRL-based covert communication precludes the use of standard handshakes, carrier synchronization, channel state estimation, and other link-maintenance operations that are taken for granted in non-covert communication. Hence, notwithstanding the progress on fundamental theory, experimental covert communication remains underexplored, with few published works focusing on optical channels [27], [53]–[55].

This paper, to our knowledge, provides the first experimental validation of the SRL on radio frequency (RF) channels. We implement and evaluate a covert communication protocol using software-defined radio (SDR). Section III-A describes our implementation, which uses USRP X310 SDR units on the COSMOS (formerly ORBIT) testbed [56], [57]. This enables controlled and reproducible experiments. We employ quadrature phase-shift keying (QPSK) with a Gaussian pulse shaping

This work was supported, in part, by the National Science Foundation under Grants No. CCF-2006679 and CNS-2107265.

The authors are with the Department of Electrical and Computer Engineering at the University of Arizona, Tucson, AZ, USA (email: {rbali, trevorbailey, bullockm, boulat}@arizona.edu)

filter. This controls temporal and spectral symbol leakage while mitigating timing jitter. We implement an experimental framework based on a synthetic Gaussian noise source within a wired, shielded network that provides environmental control and supports reproducibility.

Maintaining covert links necessitates using precise timing sources, such as atomic clocks. Furthermore, the finite resolution of modern digital transceivers' (such as SDRs) digital-to-analog and analog-to-digital converters (DACs and ADCs) imposes a fundamental *lower* limit on the amplitude of the transmitted symbol. Thus, to meet the SRL, we must use a "sparse coding" strategy, selecting a random subset of available channel uses that is secretly shared with the receiver in advance. This sparsity, in turn, renders the standard phase synchronization approaches that rely on periodic pilot signal transmission unusable. Therefore, we include a pilot signal with *every* transmitted symbol, which is done rarely if at all in non-covert communications. This, along with precise time synchronization, enables our SDR implementation to transmit a significant number of bits with a guarantee of covertness.

While we consider the worst-case adversary with complete access to the covert communication system's clock, our experiment motivates a systematic study of the impact of adversary hardware limitations, such as sampling timing jitter, as well as receiver bandwidth constraints. Furthermore, employing more efficient modulation and coding schemes (such as [58]), as well as minimizing the amount of pre-shared secret (see [9]), are avenues for future exploration. Finally, other intermittent communication systems may benefit from our approaches.

This paper is organized as follows: Section II develops the theoretical foundation for radio-frequency covert communication, beginning with the discrete-time AWGN channel model and deriving a sparse-coded QPSK transmission scheme that satisfies the SRL. Section III details our SDR implementation on the COSMOS testbed and describes the experimental procedure, while Section IV presents measurement results that validate the theory. Section V interprets these findings, highlighting practical design challenges and their implications for real-world systems, and outlines open problems and promising directions for extending this work. Finally, Appendices provide supporting derivations for the covertness criterion, phase-offset estimation, and SNR estimation used in the experiments.

II. ANALYSIS OF PRACTICAL COVERT COMMUNICATIONS

A. Channel Model

As our SDRs are digital and time-synchronized (see Section III-A for details), the discrete-time AWGN block channel model in Fig. 1 describes their input-output relationship in our physical system. A channel use corresponds to a discrete sample of Alice's input, corrupted by loss and AWGN, as observed by the legitimate receiver Bob and adversary (warden) Willie. Alice uses a discrete-time n_s -length complex-valued pulse shape $\vec{u}(x) \in \mathbb{C}^{n_s}$ to modulate data in $x \in \mathcal{X}$, where the modulation constellation \mathcal{X} is defined in Section II-B. She transmits this pulse over n_s channel uses to Bob and Willie. Bob receives $h_b \vec{u}(x) + \vec{z}^{(b)}$ while Willie observes $h_w \vec{u}(x) + \vec{z}^{(w)}$. The respective complex-valued channel gains $h_b = a_b e^{j\theta_b}$

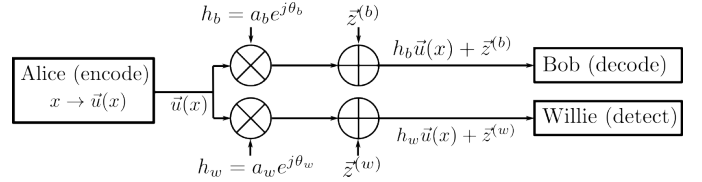


Fig. 1. Discrete-time AWGN block broadcast channel. Alice modulates $x \in \mathcal{X}$ into a complex-valued pulse shape $\vec{u}(x) \in \mathbb{C}^{n_s}$ and transmits over n_s uses of a channel corrupted by independent AWGN at legitimate receiver Bob and adversary (warden) Willie. Bob receives $h_b \vec{u}(x) + \vec{z}^{(b)}$ while Willie observes $h_w \vec{u}(x) + \vec{z}^{(w)}$, where the channel gain $h_r = a_r e^{j\theta_r}$ from Alice to the receiver $r \in \{b, w\}$ contains attenuation $a_r > 0$ and a random phase θ_r . We model noise $\vec{z}^{(r)}$ by circularly-symmetric complex Gaussian random vectors.

and $h_w = a_w e^{j\theta_w}$ contain attenuation $a_b, a_w > 0$ and phase $\theta_b, \theta_w \in [0, 2\pi]$ components. We assume channel coherence time longer than the pulse duration; thus, the channel gains h_b and h_w are constant for at least n_s AWGN channel uses. For each pulse, attenuation is arbitrary, while phase is assumed uniformly random in $[0, 2\pi]$. Each symbol in the transmitted pulse $\vec{u}(x)$ is corrupted independently by AWGN: $\vec{z}^{(b)}$ and $\vec{z}^{(w)}$ are instances of independent and identically distributed (i.i.d.) circularly-symmetric complex Gaussian random vectors $\vec{Z}^{(b)} \sim \mathcal{CN}(\vec{0}, 2\sigma_b^2 \mathbf{I}_{n_s})$ and $\vec{Z}^{(w)} \sim \mathcal{CN}(\vec{0}, 2\sigma_w^2 \mathbf{I}_{n_s})$, where \mathbf{I}_{n_s} is an $n_s \times n_s$ identity matrix.

The pulse-to-pulse variation in channel gain models the dynamic operating environment caused by the mobility of Alice, Bob, and Willie, as well as the surrounding reflecting objects. Assigning a suitable probability distribution (e.g., Rayleigh, Rice, or Nakagami) to attenuation coefficients a_b and a_w (along with uniform phase distribution) yields a corresponding block fading model (see [59, Ch. 2]). Phases θ_b and θ_w are random for each pulse slot, which captures not only environment dynamics but also the drift of independent oscillators. However, for simplicity, we assume that attenuation is constant across all channels. This models a scenario where, say, worst-case path-loss figures are employed. We defer the analysis of fully-dynamic channels to future work.

B. Practical Covert System Design

The *square root law* (SRL) governs covert communication over the AWGN channel in Fig. 1: one can transmit $B(n) = L\sqrt{n}$ covert bits reliably in n uses of such channel [1], [2], where $L > 0$ is the covert capacity (derived in [9], [10]) and $n = TW$ is the transmission time-bandwidth product. These results and much of the follow-up employ a simplified scenario with $n_s = 1$, $a_b = a_w = 1$, and $\theta_b = \theta_w = 0$. However, practical radio systems require pulse shaping to efficiently use available bandwidth and mitigate inter-symbol interference and timing jitter. Furthermore, analysis of the fundamental limits often assumes that Alice can generate inputs at arbitrarily low power. In practice, DACs and ADCs have finite resolution, which imposes a lower limit on the output signal power. We address this next, and then discuss modulation and pulse shape. Our overall system model is depicted in Fig. 2.

1) *Sparse Coding*: Divide n available channel uses into n_p pulses, with shape given by the n_s -length pulse-shape vector $\vec{u}(x)$ discussed next, $x \in \mathcal{X}$. Then, $n = n_p n_s$, with

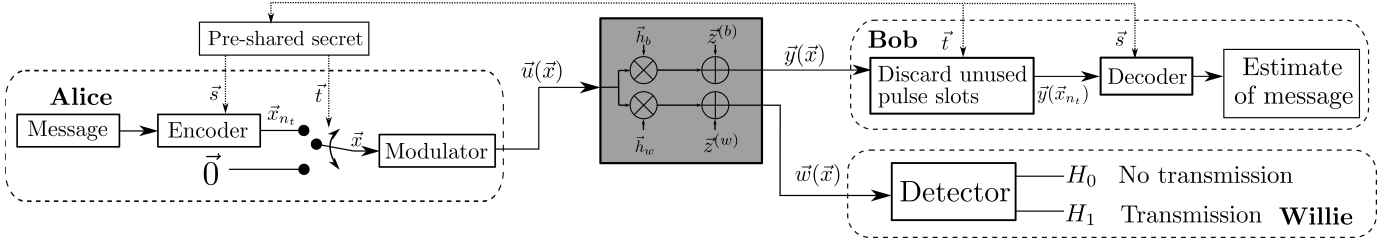


Fig. 2. System model for covert communication. Alice either encodes, modulates, and transmits a message in n_p pulses over $n = n_p n_s$ uses of the AWGN channel, or she remains silent. Here, $\vec{x} \in (\mathcal{X} \cup \{0\})^{n_p}$ is the vector of QPSK and zero symbols, with the relative location of each selected using \vec{t} . After modulation, $\vec{u}(\vec{x}) \in \mathbb{C}^n$ is the input pulse-shaped encoded signal from Alice. AWGN channel is characterized by additive noise $\vec{z}^{(w)} \in \mathbb{C}^n$ and channel gain $\vec{h}_b, \vec{h}_w \in \mathbb{C}^{n_p}$, as depicted in Fig. 1. Here, each element of \vec{h}_b, \vec{h}_w applies uniformly to one n_s sample pulse slot. Then, $\vec{y}(\vec{x}) \in \mathbb{C}^n$ (resp. $\vec{w}(\vec{x}) \in \mathbb{C}^n$) is the output at Bob (resp. Willie). Willie's goal is to determine whether Alice is transmitting. Bob and Alice use a pre-shared secret (\vec{s}, \vec{t}) to prevent this while communicating reliably.

$n_p \in \mathcal{O}(n)$. The minimum output power limit implies the norm $\|\vec{u}(x)\| = c$ for all $x \in \mathcal{X}$. We use *sparse coding* to ensure covertness: before transmission, Alice and Bob randomly generate and secretly share an n_p -length sequence \vec{t} of i.i.d. samples from the Bernoulli distribution $p(t_i) = \{1 - \alpha_n \text{ if } t_i = 0; \alpha_n \text{ if } t_i = 1\}$, where the probability of transmitting in a given slot $\alpha_n \in \mathcal{O}(1/\sqrt{n})$ follows the SRL [1], [2]. The number $n_t = \sum_{i=1}^{n_p} t_i$ of selected pulse slots is a random variable with mean $\alpha_n n_p$. It is also the length of the transmitted message \vec{x}_{n_t} , in symbols. Alice is quiet in the slots that are not selected, that is, when $t_i = 0$, she inputs $\vec{0}$. We assume that Bob and Alice are synchronized by a common clock. Denoting by $x = 0$ this ‘‘innocent’’ symbol, the transmitted symbol vector $\vec{x} \in (\mathcal{X} \cup \{0\})^{n_p}$ contains n_t symbols from \mathcal{X} and $n_p - n_t$ innocent symbols. This yields Alice's sparse-coded covert input $\vec{u}(\vec{x}) \in \mathbb{C}^n$, containing mostly innocent symbols. We derive α_n in Section II-D.

2) *Modulation and Pulse Shape*: The channel model in Section II-A includes random pulse-to-pulse phase variation. On-off keying (OOK) modulation is resilient to this as it uses energy pulses. However, OOK is power-inefficient; matching the per-symbol bit-error rate (BER) of binary and quadrature phase-shift keying (BPSK and QPSK) schemes requires transmitting twice the power, which, in turn, doubles Willie's received SNR and harms covertness. We discuss the relationship between SNR and covert signal construction further in Section II-D. We choose QPSK modulation since it doubles the number of degrees of freedom relative to BPSK, further increasing the achievable covert communication rate.

Phase variations cause errors in phase-keyed systems and are typically mitigated using periodic pilot signals; however, the SRL does not permit periodic transmissions. Furthermore, the sparse coding scheme results in the time between pulses scaling as $\mathcal{O}(\sqrt{n})$ on average, rendering the phases uncorrelated for sufficiently large n when the channel coherence time is finite. Thus, we include a fixed $n_s^{(p)}$ -length strictly-positive pilot segment \vec{c}_p in *every* transmitted pulse. For sufficiently long channel coherence time, the channel induces approximately the same phase rotation on both the pilot and data segments, preserving their relative phase. The pilot segment therefore allows estimation of the phase to correct the $n_s^{(q)}$ -length QPSK-modulated data segment $\vec{c}_q(x) = e^{\frac{j\pi(2x-1)}{4}} \vec{c}_q$, $x \in \mathcal{X}$, where $\mathcal{X} = \{1, \dots, 4\}$ and each $x \in \mathcal{X}$ is

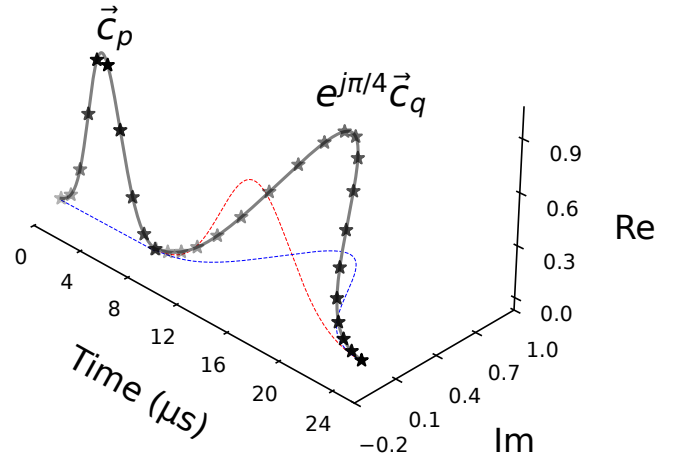


Fig. 3. Pulse shape $\vec{u}(1)$. A strictly positive pilot segment \vec{c}_p precedes the data segment \vec{c}_q , whose in-phase and quadrature components form the QPSK symbol $e^{\frac{j\pi}{4}}$ encoding $x = 1$. The projections of the complex waveform onto the real and imaginary axes are overlaid with dotted red and blue lines, respectively, and the discrete time instants at which the Gaussian envelope is sampled for transmission are marked by \star .

represented by two bits. Alice additionally applies a random phase $\theta \sim \mathcal{U}[0, 2\pi)$ to both pilot and QPSK pulse in each transmitted pulse. This improves covertness by ensuring that the relative phase between transmissions is randomized without any additional cost to decoding reliability, since Bob needs to estimate the phase anyway. Hence, the transmitted pulse is given by $\vec{u}(x) = (e^{j\theta} \vec{c}_p, e^{j\theta} \vec{c}_q(x))$ as depicted in Fig. 2, with length $n_s = n_s^{(p)} + n_s^{(q)}$ and norm $\|\vec{u}(x)\| \triangleq c$ for all $x \in \mathcal{X}$. Since the pilot requires additional power, this scheme increases Willie's received SNR. Thus, there is a trade-off between phase estimation and the covertness of our signal that we optimize in Section III-C.

Sparse coding has negligible inter-symbol interference. Instead, covertness demands energy confinement in time and frequency domains. Thus, we shape both \vec{c}_p and \vec{c}_q by a discrete-time Gaussian envelope:

$$\vec{g}_k[m] = \exp\left(-\frac{\left(m - n_s^{(k)}/2\right)^2}{2\sigma_k^2}\right), \quad m = 0, \dots, n_s^{(k)} - 1, \quad k \in \{p, q\} \quad (1)$$

and define

$$\vec{c}_k \triangleq c_k \frac{\vec{g}_k}{\|\vec{g}_k\|}, \quad k \in \{p, q\} \quad (2)$$

where σ_p , σ_q , c_p , and c_q are the corresponding pulse width and magnitude parameters. We note that more complicated pulse shapes with lower bandwidth under the same power and time constraints exist, e.g., discrete prolate spheroidal (Slepian) sequences [60, Sec. 3.1] but we defer using them to future work. In Section III-C, we optimize $n_s^{(p)}$, $n_s^{(q)}$, c_p , and c_q . Thus, we choose the largest σ_k satisfying

$$\frac{\sum_{m=0}^{n_s^{(k)}-1} \vec{c}_k[m]}{\sum_{m=-\infty}^{\infty} \vec{c}_k[m]} \geq 0.999, \quad k \in \{p, q\}, \quad (3)$$

which ensures that at least 99.9% of each pulse's energy is confined to its designated slot.

C. Reliability Analysis

Bob has \vec{t} and, thus, can discard the slots that are not used for transmission (that is, those slots corresponding to $x = 0$ in \vec{x} when Alice ‘‘transmits’’ $\vec{0}$). Thus, Bob only examines n_t pulses in $\vec{y}(\vec{x}_{n_t})$. When Alice transmits a symbol $x \in \mathcal{X}$ from \vec{x}_{n_t} in each of the n_t selected pulse slots, Bob receives the n_s -sample vector $\vec{y} = (\vec{y}_p, \vec{y}_q)$ containing two segments:

$$\vec{y}_p = a_b e^{j\theta_b} \vec{c}_p + \vec{z}_p^{(b)} \quad (4)$$

$$\vec{y}_q(x) = a_b e^{\frac{j\pi(2x-1)}{4} + \theta_b} \vec{c}_q + \vec{z}_q^{(b)} \quad (5)$$

where a_b is a constant loss, θ_b is unknown phase offset uniformly-distributed from $[0, 2\pi]$, and $\vec{z}^{(b)} = (\vec{z}_p^{(b)}, \vec{z}_q^{(b)})$ is complex-valued circularly-symmetric AWGN, per Section II-A. Bob uses \vec{y}_p to obtain the estimate $\hat{\theta}_b$ of θ_b (see Appendix II), and correct the phase of the data segment by applying $\vec{y}_q(x) e^{-j\hat{\theta}_b}$. Bob decodes the QPSK symbol by first projecting the phase-aligned data segment onto the pulse shape,

$$r_I = \left\langle \Re\{\vec{y}_q(x) e^{-j\hat{\theta}_b}\}, \vec{c}_q \right\rangle, \quad r_Q = \left\langle \Im\{\vec{y}_q(x) e^{-j\hat{\theta}_b}\}, \vec{c}_q \right\rangle. \quad (6)$$

This yields two BPSK symbols. Hard decisions $\hat{b}_1 = \text{sgn}(r_I)$ and $\hat{b}_0 = \text{sgn}(r_Q)$, followed by $\hat{b}_k = (1 - \hat{b}_k)/2$, $k \in \{0, 1\}$, extract the two bits. Since AWGN is symmetric, this hard-decision scheme induces two binary symmetric channels (BSCs) with a probability of error:

$$p_{e,\text{bsc}}^{(b)} \triangleq \Pr(\hat{b}_k = 0 \mid b_k = 1) = \Pr(\hat{b}_k = 1 \mid b_k = 0). \quad (7)$$

For sufficiently large n_p , Alice and Bob can use an error correction code (ECC) [61] on the approximately $\alpha_n n_p$ -long subset of pulse slots $\{v : t_v = 1\}$. This allows reliable transmission of

$$B_{\text{bsc}}(n) = 2n_t C_{\text{bsc}} \approx 2\alpha_n n_p C_{\text{bsc}} \quad (8)$$

bits in n channel uses on average, with $C_{\text{bsc}} \triangleq 1 - h_2(p_{e,\text{bsc}}^{(b)})$, where $h_2(p) \triangleq -p \log_2(p) - (1-p) \log_2(1-p)$ is the binary entropy function and the approximation is due to n_t being a random variable.

The ECC structure, which can aid Willie in detection, is eliminated by applying a $2n_t$ -bit one-time pad \vec{s} to the binary encoder output. Each bit in \vec{s} is selected by Alice and Bob equiprobably at random, resulting in output distribution $\Pr(x = -1) = \Pr(x = 1) = \frac{1}{2}$. Pre-shared secret includes \vec{t} and \vec{s} .

We require pre-sharing of $\mathcal{O}(\sqrt{n} \log n)$ secret key bits, since \vec{t} and \vec{s} take $n_t \log_2 n_p$ and $2n_t$ bits to represent, respectively. It is possible to reduce the required number of secret bits to $\mathcal{O}(\sqrt{n})$ at a significant complexity expense [9]. As computation uses more energy than storage, in the context of future portable covert communication systems, the logarithmic cost is worth the simplicity of our scheme.

D. Hypothesis Testing and Covertness

Willie observes the sequence $\vec{w} \in \mathbb{C}^n$ and must decide whether Alice is transmitting. Unlike Bob, he does not have access to \vec{t} and \vec{s} , but he knows the exact transmission start time and pulse boundaries. That is, Willie can access Alice and Bob's shared time, which we model in the experiment by using a common clock for all parties. Additionally, we assume that he knows the state of his channel from Alice, and other details of Alice and Bob's transceiver design (including \vec{c}_p , \vec{c}_q , and α_n). The stringency of these assumptions ensures that the system is secure against the most capable adversary. We defer studying the impact of relaxing these to future work.

Willie performs a test between binary hypotheses H_0 (silence) and H_1 (transmission). Let $P_{\text{FA}} = P(\text{choose } H_1 \mid H_0)$ and $P_{\text{MD}} = P(\text{choose } H_0 \mid H_1)$ denote the probabilities of false alarm and missed detection, respectively. Assuming non-informative priors¹ $\Pr(H_0) = \Pr(H_1) = \frac{1}{2}$, Willie's probability of error is:

$$p_e^{(w)} \triangleq \frac{1}{2} (P_{\text{FA}} + P_{\text{MD}}). \quad (9)$$

Let distributions P_0^n and P_1^n and associated density functions $p_0^n(\vec{w})$ and $p_1^n(\vec{w})$ describe the statistics of Willie's output \vec{w} when Alice is silent (H_0) and transmitting (H_1). An optimal detection scheme yields [62, Th. 15.1.1]:

$$p_e^{(w)} = \frac{1}{2} - \frac{1}{2} \mathcal{V}_T(P_0^n, P_1^n), \quad (10)$$

where $\mathcal{V}_T(P_0^n, P_1^n) \triangleq \frac{1}{2} \int_{\mathbb{C}^n} d^2 \vec{w} |p_0^n(\vec{w}) - p_1^n(\vec{w})|$ is the total variation distance between P_0^n and P_1^n . We say that the transmission is δ -covert if $p_e^{(w)} \geq \frac{1}{2} - \delta$. Total variation distance is mathematically unwieldy, hence, in covert communication literature [1], [2], [9], [10] we often employ Pinsker's inequality [8, Lemma 11.6.1] to lower bound

$$p_e^{(w)} \geq \frac{1}{2} - \frac{1}{2\sqrt{2}} \sqrt{D(P_0^n \| P_1^n)}, \quad (11)$$

where $D(P_0^n \| P_1^n) \triangleq \int_{\mathbb{C}^n} d^2 \vec{w} p_0^n(\vec{w}) \log_2 \frac{p_0^n(\vec{w})}{p_1^n(\vec{w})}$ is the relative entropy of P_0^n and P_1^n . Thus, instead of (10), one can use (11), and assert that any scheme is δ -covert if $D(P_0^n \| P_1^n) \leq \delta_{\text{RE}} = 8\delta^2$. Ultimately, satisfying this relative entropy constraint for a given δ requires limiting Alice's average output

¹Accounting for arbitrary priors is discussed in [49].

power. While relative entropy between our distributions can be readily bounded, Pinsker's inequality is loose for many distribution pairs. Thus, we seek a tighter bound than (11) to increase Alice's output power while satisfying (10). Inspired by recent work [34] that characterized covert communication over a quantum channel using quantum fidelity, we employ the classical analog of quantum fidelity to instead bound (10) [62, Th. 15.1.2] via the Cauchy-Schwarz inequality:

$$p_e^{(w)} \geq \frac{1}{2} - \frac{1}{\sqrt{2}} H(P_0^n, P_1^n) \quad (12)$$

where $H(P_0^n, P_1^n) \triangleq \sqrt{\frac{1}{2} \int_{\mathcal{C}^n} d^2 \vec{w} \left(\sqrt{p_0^n(\vec{w})} - \sqrt{p_1^n(\vec{w})} \right)^2}$ is the Hellinger distance between P_0^n and P_1^n .

Recall from Section II-B that, when transmitting, Alice inputs QPSK symbol $x \in \mathcal{X}$ in each pulse slot. Then, Willie receives $\vec{w}_p(x) = h_w \vec{u}(x) + \vec{z}^{(w)}$ for $\vec{u}(x) = (e^{j\theta} \vec{c}_p, e^{j\theta} \vec{c}_q(x))$, per the model in Fig. 1. Let $r_{p/q} = \frac{\|\vec{c}_p\|}{\|\vec{c}_q\|}$ be the ratio of magnitudes of the pilot and QPSK pulses, and $c_q = \|\vec{c}_q\|$ be the magnitude of the QPSK pulse. Appendix I shows that we ensure δ -covertness of the transmission scheme by setting

$$\begin{aligned} \alpha_n &\leq \frac{4\sqrt{2}\sigma_w^2}{a_w^2 c_q^2} \sqrt{\frac{-\log(1-2\delta^2)}{n_p(1+r_{p/q}^4)}} \\ &= \left(\text{SNR} \sqrt{1+r_{p/q}^4} \right)^{-1} \frac{4\sqrt{2}}{\sqrt{n_p}} \sqrt{-\log(1-2\delta^2)}, \quad (13) \end{aligned}$$

where $\text{SNR} \triangleq \frac{h_w^2 c_q^2}{\sigma_w^2}$ is Willie's received SNR and the penalty term $\sqrt{1+r_{p/q}^4}$ is due to inclusion of the pilot signal for channel phase estimate. Combining (13) with $n_p = n/n_s$ and (8) yields the SRL scaling of covert throughput.

E. Willie's Detectors

The preceding analysis abstracts away detector structures available to Willie. We discuss them here, deferring their analysis to Appendices III and IV.

1) *Optimal Detector*: For known densities $p_0^n(\vec{w})$ and $p_1^n(\vec{w})$, a likelihood ratio test (LRT) is optimal and achieves $p_e^{(w)}$ in (10) with equality as $n \rightarrow \infty$ [62, Th. 15.1.1]. LRT also minimizes P_{MD} for a constant P_{FA} , per Neyman-Pearson lemma [62, Th. 3.2.1]. Here, $p_0^n(\vec{w}) = \prod_{i=1}^{n_p} p^{(0)}(\vec{w}_i)$ and $p_1^n(\vec{w}) = \prod_{i=1}^{n_p} p^{(1)}(\vec{w}_i)$, with $p^{(0)}(\vec{w}_i)$ and $p^{(1)}(\vec{w}_i)$ in (18) and (19), where \vec{w}_i are the observations of the i^{th} pulse slot. Willie accuses Alice if the LRT statistic $L(\vec{w}) < 0$, where

$$L(\vec{w}) \triangleq \log \frac{p_0^n(\vec{w})}{p_1^n(\vec{w})} = \sum_{i=1}^{n_p} L_i \quad (14)$$

and $L_i = \log \frac{p^{(0)}(\vec{w}_i)}{p^{(1)}(\vec{w}_i)}$. Willie computes $L(\vec{w})$ from observations in \vec{w} given his knowledge of Alice and Bob's system. Unfortunately, Bessel functions in $p^{(1)}(\vec{w}_i)$ complicate the analysis of the resulting detector. However, we expect the QPSK pulse magnitude c_q to be small. Employing the Taylor series expansion of $L(\vec{w})$ around $c_q = 0$ in Appendix III, we simplify the LRT: Willie accuses Alice if the test statistic $S^{(\text{opt})}(\vec{w}) \geq \tau^{(\text{opt})}$, where $S^{(\text{opt})}(\vec{w}) = \sum_{i=1}^{n_p} S_i^{(\text{opt})}$,

$$S_i^{(\text{opt})} = |\langle \vec{c}_p, \vec{p}_i \rangle|^2 + |\langle \vec{c}_q, \vec{q}_i \rangle|^2, \quad (15)$$

$\vec{w}_i = (\vec{p}_i, \vec{q}_i)$ is the decomposition into pilot and QPSK segments, and $\tau^{(\text{opt})}$ is the threshold discussed later.

2) *Power Detector*: Per (15), Willie needs synchronization with Alice to use the optimal detector. Radiometer offers a practical alternative: Willie accuses Alice if the total collected power $\|\vec{w}\|^2$ exceeds the threshold $\tau^{(\text{rad})}$. For convenience, we define the radiometer test statistic $S^{(\text{rad})}(\vec{w}) = \sum_{i=1}^{n_p} S_i^{(\text{rad})}$, where $S_i^{(\text{rad})} = \|\vec{w}_i\|^2$ is in correspondence to (15).

In Appendix IV we employ the Berry-Esseen theorem to analyze the probability of error achievable by these schemes, and derive the thresholds $\tau^{(\text{opt})}$ and $\tau^{(\text{rad})}$. Furthermore, since the optimal detector achieves $p_e^{(w)}$ in (10), we show in Appendix IV-B how to improve α_n from (13) to

$$\alpha_n \leq \left(\text{SNR} \sqrt{1+r_{p/q}^4} \right)^{-1} \frac{4\sqrt{2}}{\sqrt{n_p}} \sqrt{\pi} \delta. \quad (16)$$

However, we use more conservative (13) in our experiments.²

III. EXPERIMENT IMPLEMENTATION

A. System Configuration

We perform our experiments on COSMOS (formerly ORBIT), an open-access radio grid testbed [56], [57]. Our system is depicted in Fig. 4. We connect four Ettus universal software radio peripheral (USRP) X310 SDRs, each fitted with a UBX 160 – corresponding to transmitter Alice, receiver Bob, adversary Willie, and an AWGN generator – into a shared-medium RF star network via coaxial cables. This isolates our experiment from others on COSMOS, enables control over the environment, and allows repeatability. We defer a wireless experiment with an organic noise source to future work. Our radios are not power-calibrated. Therefore, we report measurements of signal amplitude and power in arbitrary units, respectively denoted as a.a.u. and a.p.u. The radios are positioned so that Bob and Willie experience approximately equal attenuation from both the AWGN generator and Alice, corresponding to an adverse scenario in which Willie is close to Bob. We utilize a single 12.5 MHz channel centered at $f_c = 915$ MHz. Both the transmitting (Alice and noise generator) and receiving (Bob and Willie) radios are offset-tuned by 25 MHz.

Each radio has a dedicated enhanced small form-factor pluggable (SFP+) cable connecting it to a high-bandwidth router, and the router to a dedicated control node on the COSMOS grid [57]. SFP+ ports operate at 10 Gbps to support a maximum transmission unit (MTU) of 8 kB. This prevents packet drops due to an internal radio buffer overflow during an experiment. We note that even a single packet drop can cause catastrophic misalignment of the covert symbols during transmission, rendering an entire experimental trial useless. COSMOS provides a network [57] connecting the control nodes to network attached storage (NAS) and to other nodes forming a compute cluster for processing the collected data.

The radios' internal clocks are synchronized using an Ettus OctoClock, which provides low-jitter pulse-per-second (PPS)

²An anonymous referee's final review comment led to (16). Regrettably, the publication deadline prevented us from using it in our experiments.

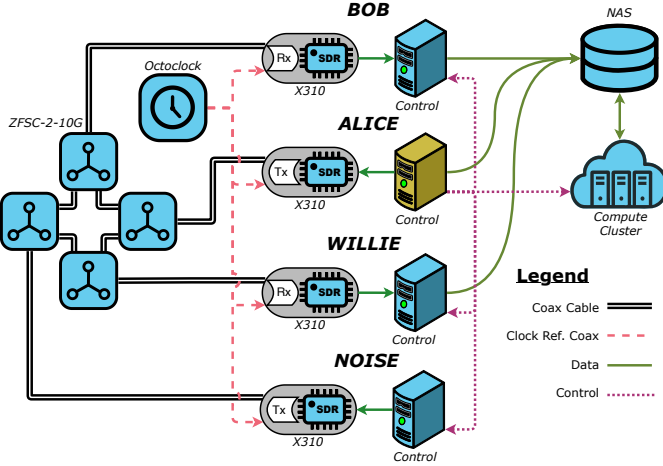


Fig. 4. Covert communication experiment on COSMOS. Four Ettus USRP X310 radios – Alice (Tx), Bob (Rx), Willie (warden), and a broadband noise source – are linked by coaxial cables in a star topology using Mini-Circuits ZFSC-2-10G splitters/combiners. Tx-to-Rx and Tx-to-Tx path losses are 50 dB and 65 dB, respectively. All radios operate at $f_c = 915$ MHz with Alice, Bob, and Willie using a DAC/ADC sampling rate of $f_s = 12.5 \times 10^6$ samples/s and the noise generator $f_s = 22.5 \times 10^6$ samples/s. Alice, Bob, and Willie apply 0 dB Tx/Rx gain while the noise generator applies 15 dB gain. Each X310 connects over a 10 Gb/s SFP+ link to a dedicated control node (Intel Xeon E5-2640, 20 cores); Alice’s node orchestrates the experiment via TCP messages to the other nodes and an eleven-node compute cluster of the same machines that performs real-time processing, while a 2 TB network-attached storage (NAS), mounted via NFS v4.2, provides a shared buffer.

and 10 MHz reference signals, allowing the radios to maintain a constant phase offset between each other [63]. We note that a centralized clock source is merely an experimental convenience. In practice, Alice, Bob, and Willie can synchronize *independently* to any stable clock source, such as an atomic clock, prior to transmission.³

Alice’s node generates fresh pre-shared secret and message vectors \vec{t} and \vec{x}_{2n_t} for each experimental trial. Bob and Willie’s radios continuously sample the channel, while Alice supplements the RF trial packet described in Section III-D with TCP control messages over the SFP+ connections that mark its precise start and stop times. At the end of each trial, control nodes write their data to the network-attached storage (NAS): Alice’s node stores \vec{t} and \vec{x}_{2n_t} , whereas Bob and Willie’s nodes write their raw IQ samples, padded with brief pre- and post-buffers. Alice’s node then alerts the compute cluster, which analyzes the new trial and deletes its data on completion. Acting as a rolling buffer, the NAS keeps heavy data traffic off the radio-control links and holds disk usage well below its 2 TB capacity. The Ettus USRP library and USRP hardware driver (UHD), [64], [65] are used to interact with the radios.

B. Alice’s Spectral Footprint and SDR Non-idealities

Section II-D addresses the fundamental limitations of implementing covert communication on digital transceivers. Here, we identify the constraints specific to our SDR platform.

Our analysis assumes that Alice’s signal energy is confined to a single 12.5 MHz channel. In practice, this is often

³In a separate experiment in our lab at the University of Arizona, we confirmed this using a Stanford Research Systems FS725 10 MHz Rubidium Frequency Standard connected to Ettus USRP N210 radios.

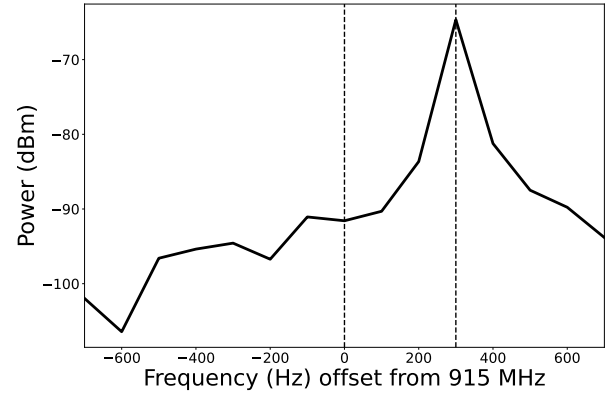


Fig. 5. Measured spectrum at Willie’s receiver. The Gaussian main lobe, expected to be centered at 915 MHz, is displaced by approximately +300 Hz, indicating a small carrier-frequency offset.

violated: time-limited signals are unbounded in the frequency domain, and transmitter hardware non-idealities can generate strong spectral artifacts. To characterize the emitted spectrum, we capture Alice’s waveform with a Tektronix RSA5115B real-time spectrum analyzer positioned at Willie’s location to record his observations exactly. The analyzer is centered at 915 MHz, samples at 2×10^8 samples/s, and the external AWGN generator remains disabled throughout these spectral measurements. Alice transmits the shortest Gaussian pulses permitted by the system, $n_s^{(p)} = n_s^{(q)} = 6$, at an amplitude of $m_p = 0.12351232$, $m_q = 1.3313578$.

Fig. 5 plots the spectrum obtained by integrating over many successive pulses; the Gaussian main lobe is shifted by roughly +300 Hz from the nominal 915 MHz. This offset exceeds the datasheet specification for a GPS-disciplined 10 MHz reference, which claims a frequency accuracy of ± 25 parts per billion (ppb), or ± 23 Hz at 915 MHz [66].

Fig. 6(a) overlays the pilot-data pulse pair at the transmitter with the corresponding waveform captured by the spectrum analyzer; the traces align closely, confirming that the temporal shape is maintained. Fig. 6(b) presents the received spectrum over a wide frequency span and includes an inset that zooms to the carrier band observable at the transmitter. The transmit and receive spectra are overlaid in the inset and coincide nearly identically, confirming that the Gaussian envelope and its 99.9% energy bandwidth are maintained. The full-span view further shows that essentially all energy is confined to this zoomed region; only a few narrow spikes appear in the immediate vicinity of the band edges, and with a single capture, it is unclear whether these are random artifacts or a repeatable spectral feature.

Farther out in frequency, Fig. 7(a) shows two pronounced spurs at the third and fifth harmonics of the carrier. Odd harmonics typically arise when a nominally sinusoidal signal develops a more square-like waveform, which in a transmitter can happen either through power-amplifier compression or through non-sinusoidal drive in the local oscillator (LO) chain. Neither explanation fits neatly here: the measurement is made at 0 dB hardware gain, well below the power amplifier’s compression point, and the UBX-160 LO path is followed

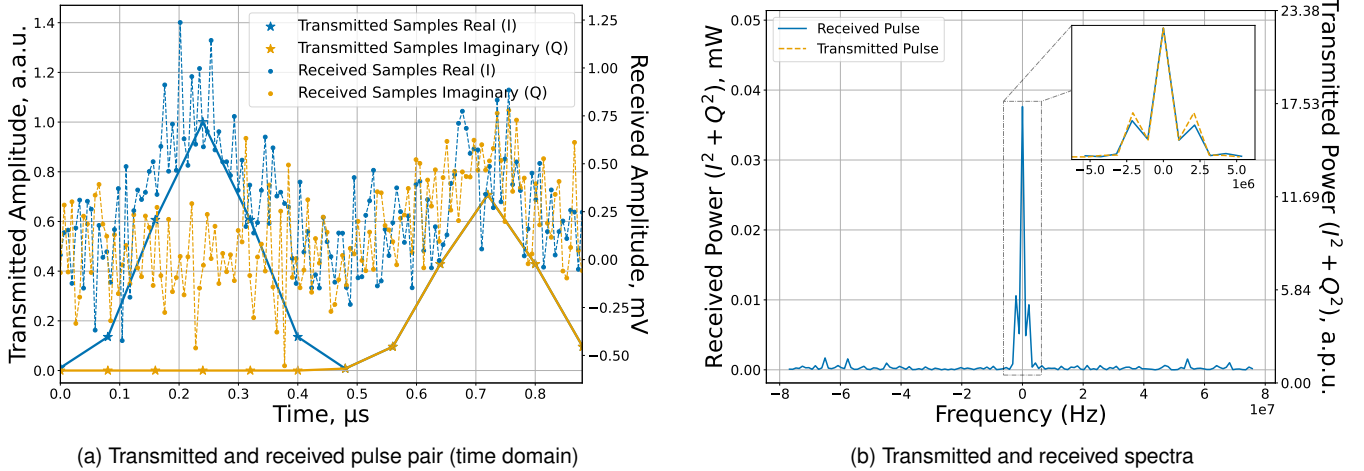


Fig. 6. Carrier-band verification of the 12-sample pulse pair transmitted by Alice at 0 dB gain. Each pair comprises a 6-sample Gaussian pilot followed immediately by a 6-sample Gaussian QPSK-data pulse. The left panel overlays the time-domain waveforms at the transmitter and at a spectrum analyzer placed at Willie, while the right panel shows the spectrum analyzer output, with insets overlaying the transmitted and received spectra in the carrier band. The amplitude and power transmitted by our uncalibrated radio are in arbitrary amplitude and power units (a.a.u. and a.p.u.).

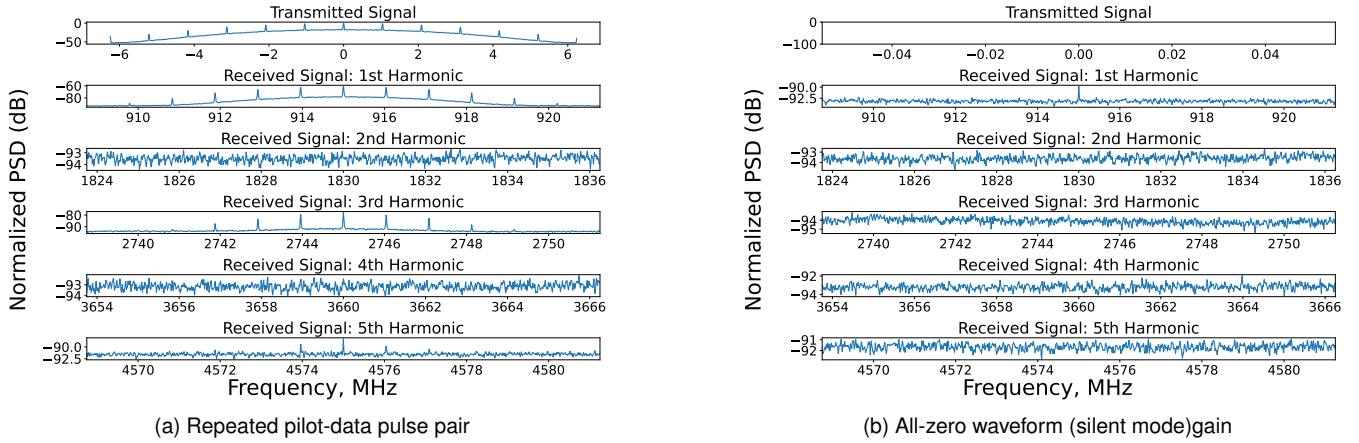


Fig. 7. Spectra at the first five harmonics, measured at Willie with Alice’s transmitter gain set to 0 dB. Left: when Alice continuously repeats the pilot-data pulse pair. Right: when the baseband input is forced to all zeros (silent mode). The ordinate scale is in dB relative to peak transmitted power.

by a 2.2 GHz low-pass section that should strongly attenuate components at 2.75 GHz and 4.58 GHz. The precise mechanism that leaves these third- and fifth-harmonic spurs above the noise floor, therefore, should be investigated.

To verify that Alice’s silent mode is truly quiet, we transmit an all-zero waveform. Even with an all-zero signal, the spectrum in Fig. 7(b) shows a small spur at the carrier and faint harmonics, behavior attributable to LO leakage.

The two spectral artifacts most relevant to covertness at the settings used in our experiments are (i) the power that spills into odd harmonics and (ii) the residual carrier spur that appears when Alice is commanded to remain silent. The former could be mitigated by inserting an external low-pass filter at Alice’s RF output, while the latter may be reduced through a careful power calibration of the X310 transmit chain. Making these improvements is challenging on shared-testbed hardware with limited on-site access. We will pursue this in the follow-on work.

The radio circuitry is always on in our experiments. How-

ever, prior theoretical work and the analysis in Section II effectively assume that Alice’s transmitter is completely powered off unless it is transmitting a pulse. In practice, power cycling a radio consumes significant time and may emit unwanted signals. That being said, we will investigate powering it off in the future, as the long intervals between sparse-coded transmissions may permit it. Furthermore, in some practical scenarios, H_0 can correspond to Alice’s transmitter being always on but transmitting zero, as in our implementation.

Finally, LO power leaks into the baseband due to imperfect isolation between the LO and RF ports. When combined with small frequency offsets of the LO from the desired center frequency f_c , this leakage manifests as high-amplitude low-frequency noise. To mitigate this, we offset-tune our radios by 25 MHz, shifting the signal of interest away from this DC-centered noise.

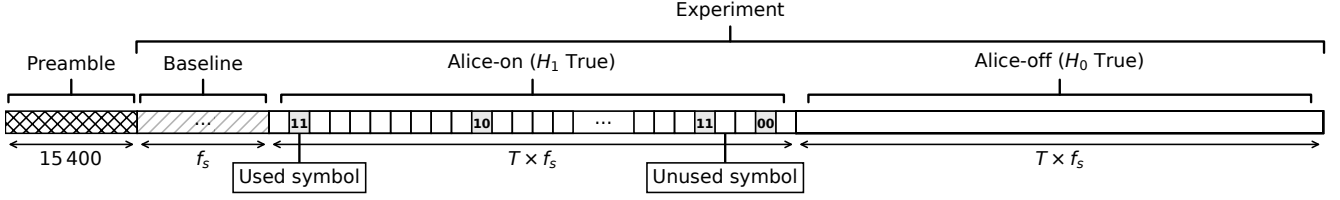


Fig. 8. Data-packet structure (durations in samples). A 15400-sample preamble is created by concatenating five 13-bit Barker sequences, BPSK-modulating them, zero-padding each to 200 samples, and convolving the result with a 2401-sample root-raised-cosine filter. This is immediately followed by a one-second (f_s -sample) silence interval to measure the baseline noise level. The subsequent T -second, $T \times f_s$ -sample segments encode the two parts of the experimental trial. In the Alice-on segment, each shaded pulse slot begins with a strictly positive, real-valued Gaussian pilot pulse (for phase reference), immediately followed by a Gaussian-shaped, QPSK-modulated data pulse carrying randomly generated information bits. The indices of the occupied slots are drawn uniformly at random and stored in \vec{t} (see Section II-C). In the subsequent Alice-off segment, she remains silent.

C. Pulse Optimization

To maximize the number of covert bits that can be reliably conveyed, we jointly tune four pulse-design parameters: the pilot-pulse length $n_s^{(p)}$, data-pulse length $n_s^{(q)}$, pilot-pulse magnitude c_p , and data-pulse magnitude c_q . We model the relationship between these parameters and the attainable covert bit count as a black-box objective, apply Bayesian optimization to efficiently navigate the parameter space, and use our hardware testbed to measure the covert bits delivered for each candidate configuration. Bayesian optimization iteratively explores the four-dimensional design space $\vec{d} = (n_s^{(p)}, n_s^{(q)}, c_p, c_q)$ by maintaining a *surrogate model* of the unknown mapping from \vec{d} to attainable covert bit count. We leverage the Ax library in Python [67] to perform this optimization. The three steps that follow are the standard Bayesian optimization loop [68, Ch. 31]; we restate them here.

- **Propose**: a new configuration \vec{d}_u is generated from the surrogate using all observations collected so far.
- **Measure**: using \vec{d}_u , the radio transmits a modified version of the data packet (Section III-D): every fifth pulse slot in the Alice-on segment carries a random bit, and the Alice-off segment is removed. The number of attainable covert bits is recorded over 100 one-second trials. The average number of attainable covert bits for a given parameter set is $r = 2 C_{\text{bsc}} n_p \alpha_n$ bits over n uses of the channel. Here, n corresponds to the number of samples available in a one-second transmission. This yields a sample mean, \bar{r}_u , and a standard error, $s_{\bar{r}_u}$.
- **Update**: the tuple $(\vec{d}_u, \bar{r}_u, s_{\bar{r}_u})$ is appended to the data set and the surrogate is refitted before the next proposal.

After 200 iterations we use $\vec{d}^* = \arg \max_{1 \leq l \leq 200} \bar{r}_l$, the configuration with the highest observed mean throughput.

We use a Gaussian-process surrogate, which is commonly adopted in Bayesian optimization. We briefly review it here. For a set of l different input parameter configurations $\vec{d}_{1:l} = [\vec{d}_1, \vec{d}_2, \dots, \vec{d}_l]$, the model predicts l corresponding covert throughput values sampled from the distribution $\mathcal{GP}(0, k(\vec{d}_{1:l}, \vec{d}_{1:l}))$ [69], where k is a covariance function, which is the Matérn-5/2 function [69, Ch. 4] here. This model can also be used to predict the throughput given priors, i.e., given $u - 1$ tuples $(\vec{d}, \bar{r}, s_{\bar{r}})$, the model predicts the throughput \hat{r}_u for some new parameter set \vec{d}_u . This prediction

is distributed as $\hat{r}_u \mid \bar{r}_{1:(u-1)}, \vec{d}_{1:u}, s_{\bar{r}_{1:(u-1)}} \sim \mathcal{N}(\mu_u, \sigma_u^2)$, where μ_u and σ_u can be directly calculated. At iteration u , configuration \vec{d}_u that maximizes *expected improvement* $\mathbb{E}[\hat{r}'_u \mid \hat{r}'_u > \bar{r}_{1:(u-1)}^*]$ for a candidate parameter configuration \vec{d}'_u is proposed for measurement, where $\hat{r}_{1:(u-1)}^*$ is the highest measured throughput for the first $u - 1$ trials, i.e., $\bar{r}_{1:(u-1)}^* = \max_{1 \leq v \leq (u-1)} \bar{r}_v$.

The resulting optimum ($n_s^{(p)} = 26, n_s^{(q)} = 34, c_p = 2.9765, c_q = 3.521$) is adopted for the experiments that follow.

D. Transmission Structure for Experimental Trials

In each experimental trial, Alice transmits the four-segment packet shown in Fig. 8: a non-covert *preamble*, a baseline-estimation gap, an *Alice-on* segment, and an *Alice-off* (noise-only) segment. An AWGN generator operates continuously throughout the experiment. The Alice-on and Alice-off segments last T seconds each, while the preamble marks the start of each trial and facilitates finding Alice's transmission in Bob's and Willie's traces.

The preamble consists of the 13-bit Barker sequence repeated five times (65 bits in total). Each bit is BPSK-modulated and occupies 200 samples; the first sample carries the modulated symbol, followed by 199 zero-padding samples. The resulting 13000-sample sequence is then pulse-shaped with a root-raised-cosine (RRC) filter with roll-off factor $\beta = 0.35$, spanning 12 symbols and represented digitally by $12 \times 200 + 1 = 2401$ taps. After filtering, the preamble length is $65 \times 200 + (2401 - 1) = 15,400$ samples. The baseline-estimation gap is one second (f_s -samples) long, and is used to monitor noise power level throughout the experiment.

During the Alice-on segment, Alice embeds her covert message using the pilot- and data-pulse pairs defined in Section 2, transmitting only in the pulse slots indexed by \vec{t} . We evaluate covert throughput and Bob's decoding reliability, as well as Willie's detection performance under hypothesis H_1 , using the Alice-on segment. The Alice-off segment, which contains only AWGN, is used to characterize Willie's detector under the null hypothesis H_0 .

E. Experiment design

We select eight logarithmically-spaced values of Alice's transmission duration $T \in [10^{-0.3}, 10^{0.75}]$ s. For each value

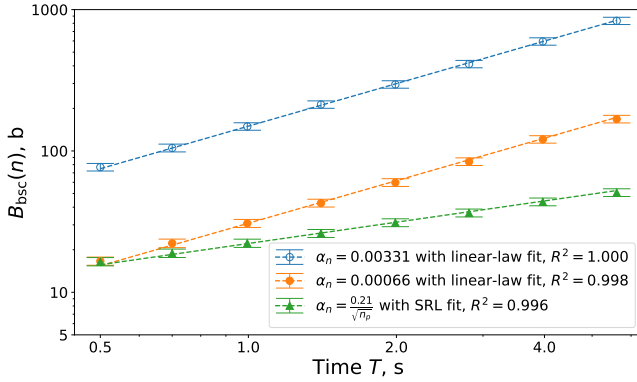


Fig. 9. Bob’s receiver performance. We plot the total number $B_{\text{bsc}}(n)$ of reliably-decodable bits for $n = f_s T$ channels uses vs. transmission duration T on a log-log scale, with 95% confidence intervals as error bars give $N = 10^3$ trials per datapoint. R^2 is the coefficient of determination.

of T , we conduct $N = 10^3$ independent trials using distinct transmission packets described in Section III-D. Before we begin our experiment, we estimate Willie’s SNR using a 20 two-second calibration transmission with a modified version of the data packet from Section III-D: every fifth pulse slot in the Alice-on segment is used to transmit a random bit, and the Alice-off segment is deleted. The SNR is computed from the mean power values of the pilot, pulse, and noise, and the full estimator is detailed in Appendix VI. We use the SNR estimate to compute $\zeta = \alpha_n \sqrt{n} =$, where $n = n_p n_s$ and α_n is in (13). We set $\delta = 0.07$ and use the result to compute α_n for each value of T . This models Alice following the SRL. We also evaluate two scenarios when Alice carelessly does not follow the SRL, where $\alpha_n = \{6.6 \times 10^{-4}, 3.31 \times 10^{-3}\}$, the first corresponding to α_n for the SRL at $T = 10^{-0.3}$ s. We use these three values of α_n to generate random vectors \vec{t} with pulse locations used by Alice to transmit for each trial.

IV. RESULTS

A. Covert Throughput

Fig. 9 plots Bob’s receiver’s performance vs. transmission duration T . Bob uses \vec{t} to estimate bits only at the pulse locations Alice uses for transmission, per the sparse coding described in Section II-C. We report the estimates of the total number of transmissible covert bits $B_{\text{bsc}}(n)$ by averaging over $N = 10^3$ trials using the equality in (8). Per Section III-E, Alice either follows the SRL or does not. We fit lines with slopes of either one-half or unity to the corresponding log-log plot results. We calculate the coefficient of determination R^2 , which is the proportion of the variation in $B_{\text{bsc}}(n)$ explained by the square-root or linear dependence on T [70, Ch. 1.3]. Our values of $R^2 > 0.99$ indicate the scaling results that we anticipate. While careless Alice can transmit significantly more bits, this makes her detectable, as discussed next.

B. Detectability

We employ two methods to assess the detectability of Alice’s transmission: directly by using a constant false-alarm rate (CFAR) strategy, and by evaluating the probability of error

$p_e(w)$ in (9). For both approaches, we use the optimal detector and the radiometer discussed in Section II-E. We consider a scenario where the noise power level is static, which favors Willie. We leave the extension to a dynamic environment, which could significantly favor Alice [49], for future work.

1) *CFAR Strategy*: Suppose Willie has a fixed false alarm budget P_{FA}^* and can collect detector data when Alice is absent. He then estimates a CFAR threshold on his test statistic. We implement this as follows: for a each value of T , and each detector in Section II-E, we find a threshold τ^* on a test statistic S such that the number of trials where $S > \tau^*$ given H_0 (i.e., the false alarm events) is $P_{\text{FA}}^* N$. Thus, τ^* corresponds to a threshold that yields empirical false alarm probability $P_{\text{FA}} = P_{\text{FA}}^*$. We then report the corresponding fraction of trials when $S \leq \tau^*$ given H_1 , which estimates the probability of missed detection P_{MD} . We note that our estimates of P_{MD} and its 95% confidence intervals depend on τ^* . It, in turn, depends on the measured noise power level, which is random. However, tight control of our environment and a large number of trials used to calculate τ^* render it nearly deterministic. Fig. 10 presents the results for $P_{\text{FA}}^* = 0.1$. We compare the detectors at the end of this section.

2) *Evaluation of $p_e^{(w)}$* : Fig. 11 presents our estimates of Willie’s probability of error $p_e^{(w)}$ in (9). First, we obtain the lower bound on $p_e^{(w)}$ when Alice follows the SRL by computing the upper bound on the Hellinger distance between the probability distributions of his received signals under each hypothesis in Appendix I. This is, effectively, a lower bound (12) on a lower bound (10). We estimate the SNR for each trial as described in Appendix VI, calculate the bound, and plot the average over $N = 10^3$ trials on both subfigures in Fig. 11. The correspondence to the covertness requirement $p_e^{(w)} \geq \frac{1}{2} - \delta = 0.43$ indicates that our system operates as expected and that the noise power level and loss are stable throughout our experiments.

We also investigate the performance of the optimal detector and radiometer described in Section II-E. For each trial, we estimate the threshold $\frac{\sqrt{n_p} \Delta \mu}{\sigma_0 + \sigma_1}$ for each detector using Willie’s observations as described in Appendix VI and calculate the estimate for $p_{e,\text{det}}^{(w)}$ using (36). This corresponds to Willie implementing the detectors using information on the squared magnitude $a_w^{(w)}$ of the gain on his channel from Alice (which we assume he has), as well as measurements of the background noise σ_w^2 . We note that the Berry-Esseen estimation errors $\epsilon_{n_p,0}$ and $\epsilon_{n_p,1}$ are negligible due to n_p being large. We report the averages for each detector over $N = 10^3$ trials.

3) *Detector Comparison*: Both strategies show that Willie’s probability of error remains constant when Alice follows the SRL. When Alice is careless, the optimal detector’s probability of error decays fairly rapidly with time T . On the other hand, the radiometer does not perform well in our experiments, even when α_n is a constant (corresponding to careless Alice).⁴ Nevertheless, this demonstrates how Alice can exploit shortcomings in Willie’s detector design to improve her covert communication capabilities.

⁴In a separate experiment we used a larger constant α_n , and confirmed that radiometer detects careless Alice.

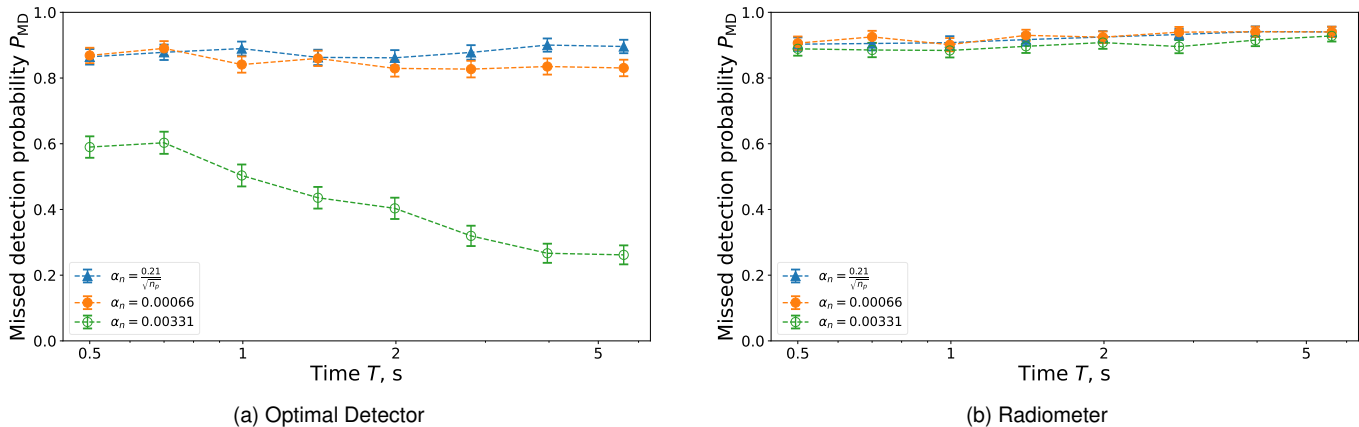


Fig. 10. Comparison of missed detection probability p_{MD} under CFAR $P_{FA}^* = 0.1$ vs. transmission duration T (log scale) for (a) the optimal detector and (b) the radiometer. Results are averaged over $N = 10^3$ trials with 95% confidence intervals shown.

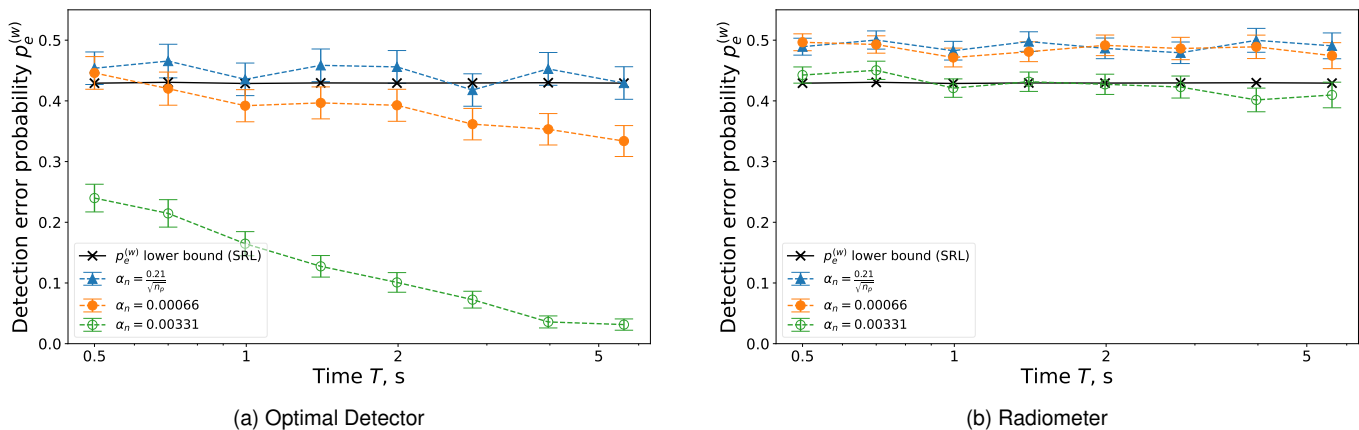


Fig. 11. Comparison of detection error probability $p_e^{(w)}$ versus transmission duration T (log scale) for (a) the optimal detector and (b) the radiometer. Results are averaged over $N = 10^3$ trials with 95% confidence intervals shown. The analytical lower bound from (12) is calculated using the power from the same trials, but its error bars are negligible and omitted for clarity.

V. CONCLUSION, DISCUSSION, AND FUTURE WORK

We demonstrate the first implementation of SRL-based covert communication in the RF domain. We employ SDRs, which are not specifically designed for covert communication. We have to address significant challenges:

- *Dynamic range and ADC/DAC granularity limitations:* The UBX-160 daughterboards use a 16-bit DAC for transmission and a 14-bit ADC for reception. While Alice can generate high-resolution low-power pulses, Bob's lower ADC precision limits his ability to distinguish weak signals from noise. Ensuring pulse detection after digitization requires minimal transmission power, which necessitates sparse coding. This, in turn, needs tight time synchronization, which we demonstrate.
- *Time and frequency synchronization:* The oven-controlled crystal oscillators (OCXOs) in USRP X310s lack the frequency accuracy and stability needed to decode sparsely transmitted covert symbols. Furthermore, Bob has to know precisely when Alice begins transmitting. We use a common reference (OctoClock) and a non-covert preamble; however, in practice, GPS or a highly stable time

source, such as an atomic clock, can be used for both disciplining the local oscillators and for timing information. We will employ these in follow-on experiments.

- *Data volume:* Our capture for $N = 10^3$ trials amounts to approximately 72 h of baseband data at a sampling rate of $f_s = 12.5$ MHz, using 64-bit in-phase and quadrature samples for each receiver (Bob and Willie). This produces roughly 10 TB of data. Although real-time processing is performed on the compute cluster, both computational and storage demands must be reduced for practical deployment.
- *Continuous noise injection:* Maintaining an always-on, spectrally flat artificial noise floor is limited by the maximum DAC sampling rate the system can sustain: sampling too fast can overwhelm the host CPU and lead to buffer under-flows. In the future, we will explore using multiple radios to emulate noise and more natural noise sources by experimenting “in the wild.”

Indeed, our proof-of-concept experiment raises many theoretical and experimental research questions. In the short term, we plan to address some of them by improving our COSMOS-

based design as follows:

- We will add control over path loss to study the impact of channel dynamics;
- We will look for an optimal constellation satisfying the covertness criteria in (10) and (12). There is evidence for this being QPSK, as it is optimal for complex-valued circularly-symmetric AWGN under the criterion in (11) (by extending the BPSK case for real-valued AWGN channels in [2], [9], [10]). This is also actively investigated in quantum information theory [34].

Additionally, the AWGN channel model provides only a zeroth-order approximation to practical RF channels. Thus, SRL-based covert communication needs to be validated in a more realistic, dynamic environment. We plan on evolving our system to be independent rather than centrally controlled. This would allow not only experimentation “in the wild” but also exploration of covert networks. Furthermore, we plan to relax the assumption on the adversary’s capabilities and study the impact of, e.g., the lack of precise knowledge of the timing of transmission and the pulse shape used.

ACKNOWLEDGMENT

The authors are grateful to Ivan Seskar and the COSMOS staff for setting up the radios on COSMOS and answering our many questions. The authors thank Loukas Lazos, Ming Li, Jingcheng Li, Ziqi Xu, Samuel H. Knarr, and Timothy C. Burt for valuable advice and for sharing the equipment. The authors also acknowledge helpful discussions with Mark J. Meisner, Jaim Bucay, Dennis L. Goeckel, Donald F. Towsley, Matthieu R. Bloch, Matthew Arcarese, and Robert J. McGurrian. Finally, the authors thank the anonymous referees for their suggestions, which substantially improved the manuscript.

APPENDIX I COVERTNESS CRITERION ANALYSIS

Since Willie knows the start time, the duration of Alice’s transmission, and details of her system from Section II-C, he collects n observations corresponding to the total number of channel uses available to Alice. Furthermore, Alice randomizes the per-pulse phase θ since her pilot-aided QPSK scheme allows Bob to recover phase information on receive without further channel estimation. These n observations are divided into n_p pulse slots of $n_s = n_s^{(p)} + n_s^{(q)}$ observations each, corresponding to pulses containing $n_s^{(p)}$ (resp. $n_s^{(q)}$) samples of pilot signal (resp. QPSK symbol), as described in Section II-C. Each density function $p^{(h)}(\vec{w}_i)$ with segment $\vec{w}_i \in \mathbb{C}^{n_s}$ is indexed according to the true hypothesis H_h , $h \in \{0, 1\}$ and pulse location $i = 1, \dots, n_p$. For hypothesis H_1 when Alice employs a pilot signal, we decompose $\vec{w}_i = (\vec{p}_i, \vec{q}_i)$ for pilot samples $\vec{p}_i \in \mathbb{C}^{n_s^{(p)}}$ and QPSK samples $\vec{q}_i \in \mathbb{C}^{n_s^{(q)}}$, respectively. Denote by $\psi(\vec{w}; \vec{\mu}, \mathbf{\Gamma}, \mathbf{C})$ the multi-dimensional complex Gaussian density function with mean vector $\vec{\mu} =$

$E[\vec{W}]$, covariance matrix $\mathbf{\Gamma} = E[(\vec{W} - \vec{\mu})(\vec{W} - \vec{\mu})^\dagger]$, and relation matrix $\mathbf{C} = E[(\vec{W} - \vec{\mu})(\vec{W} - \vec{\mu})^T]$, defined as

$$\psi(\vec{w}; \vec{\mu}, \mathbf{\Gamma}, \mathbf{C}) = \frac{\exp\left(-\frac{1}{2} \begin{bmatrix} \vec{w} - \vec{\mu} \\ \vec{w} - \vec{\mu} \end{bmatrix}^\dagger \begin{bmatrix} \mathbf{\Gamma} & \mathbf{C} \\ \mathbf{C} & \mathbf{\bar{\Gamma}} \end{bmatrix}^{-1} \begin{bmatrix} \vec{w} - \vec{\mu} \\ \vec{w} - \vec{\mu} \end{bmatrix}\right)}{\pi^n \sqrt{\det(\mathbf{\Gamma}) \det(\mathbf{\bar{\Gamma}} - \mathbf{C}^\dagger \mathbf{\Gamma}^{-1} \mathbf{C})}}, \quad (17)$$

where $\mathbf{\bar{A}}$ denotes the complex conjugate of matrix \mathbf{A} . Since our noise is i.i.d. and induces circularly symmetric complex Gaussian distributions, $\mathbf{C} = \mathbf{0}$ and we drop it for brevity. Under H_0 , Alice does not transmit and Willie observes AWGN. Thus, segments are i.i.d. with the density function:

$$p^{(0)}(\vec{w}_i) = \psi(\vec{w}_i; \vec{0}, 2\sigma_w^2 \mathbf{I}_{n_s}). \quad (18)$$

Alice transmits under hypothesis H_1 . Since Willie does not have \vec{t} and \vec{s} , segments are i.i.d. with the density function:

$$\begin{aligned} p^{(1)}(\vec{w}_i) &= \int_0^{2\pi} d\theta \left((1 - \alpha_n) \psi(\vec{w}_i; \vec{0}, 2\sigma_w^2 \mathbf{I}_{n_s}) \right. \\ &\quad \left. + \frac{\alpha_n}{4} \sum_{x=0}^3 \psi(\vec{w}_i; e^{j\theta} \vec{\mu}(x), 2\sigma_w^2 \mathbf{I}_{n_s}) \right) \\ &= (1 - \alpha_n) \psi(\vec{w}_i; \vec{0}, 2\sigma_w^2 \mathbf{I}_{n_s}) \\ &\quad + \frac{\alpha_n}{4} \sum_{x=0}^3 \int_0^{2\pi} d\theta \psi(\vec{p}_i; e^{j\theta} h_w \vec{c}_p, 2\sigma_w^2 \mathbf{I}_{n_s}) \\ &\quad \times \psi(\vec{q}_i; e^{j(\theta + \pi \frac{2x-1}{4})} h_w \vec{c}_q, 2\sigma_w^2 \mathbf{I}_{n_s}) \\ &= (1 - \alpha_n) \psi(\vec{w}_i; \vec{0}, 2\sigma_w^2 \mathbf{I}_{n_s}) \\ &\quad + \frac{\alpha_n}{4} \psi(\vec{w}_i; \vec{0}, 2\sigma_w^2 \mathbf{I}_{n_s}) e^{-a_w^2 \frac{\|\vec{c}_p\|^2 + \|\vec{c}_q\|^2}{2\sigma_w^2}} \\ &\quad \times \sum_{x=0}^3 I_0\left(\frac{a_w}{\sigma_w^2} f_x(\vec{w}_i, \vec{c}_p, \vec{c}_q)\right), \end{aligned} \quad (19)$$

where $I_0(\cdot)$ is the modified Bessel function of the first kind with order 0, a_w is the channel loss, and

$$\begin{aligned} f_k(\vec{w}_i, \vec{c}_p, \vec{c}_q) &= \left(\left(\langle \vec{c}_p, \Re(\vec{p}_i) \rangle + (-1)^{\lfloor k/2 \rfloor} \langle \vec{c}_q, \Re(\vec{q}_i) \rangle \right)^2 \right. \\ &\quad \left. + \left(\langle \vec{c}_p, \Im(\vec{p}_i) \rangle + (-1)^k \langle \vec{c}_q, \Im(\vec{q}_i) \rangle \right)^2 \right)^{1/2} \end{aligned} \quad (20)$$

We seek to bound Willie’s probability of detection error. Cauchy-Schwarz inequality implies $\mathcal{V}_T(P_0^n, P_1^n) \leq \sqrt{2} H(P_0^n, P_1^n)$, thus we analyze the Hellinger distance between our distributions. We have

$$\begin{aligned} H^2(P_0^n, P_1^n) &= 1 - \int_{\mathbb{C}^{n_s}} d^2 \vec{w}_i \sqrt{\prod_{i=1}^{n_p} p^{(0)}(\vec{w}_i) p^{(1)}(\vec{w}_i)} \end{aligned} \quad (21)$$

$$= 1 - \prod_{i=1}^{n_p} \int_{\mathbb{C}^{n_s}} d^2 \vec{w}_i \sqrt{p^{(0)}(\vec{w}_i) p^{(1)}(\vec{w}_i)} \quad (22)$$

$$= 1 - \left(\int_{\mathbb{C}^{n_s}} d^2 \vec{w}_1 \sqrt{p^{(0)}(\vec{w}_1) p^{(1)}(\vec{w}_1)} \right)^{n_p} \quad (23)$$

The term inside the power of n_p on the right hand side of (23) admits no known closed-form expression, so we take its Taylor series expansion. Without loss of generality, substitute $\vec{c}_q \rightarrow c_q \vec{b}_q$ where $c_q = \|\vec{c}_q\|$ is the magnitude of the QPSK pulse and $\|\vec{b}_q\| = 1$ is the unit vector with the same pulse shape as \vec{c}_q . Similarly, substitute $\vec{c}_p \rightarrow c_q r_{p/q} \vec{b}_p$ where $r_{p/q} = \frac{\|\vec{c}_p\|}{\|\vec{c}_q\|}$ is the ratio of magnitudes the pilot pulse and the QPSK pulse, and $\|\vec{b}_p\| = 1$ is the unit vector with the same pulse shape as the \vec{c}_p . We Taylor expand the term inside the power of n_p about $c_q = 0$, and obtain:

$$\begin{aligned} & \int_{\mathbb{C}^{n_s}} d^2 \vec{w}_1 \sqrt{p^{(0)}(\vec{w}_1) p^{(1)}(\vec{w}_1)} \\ &= 1 - \alpha_n^2 \frac{1 + r_{p/q}^4}{32\sigma_w^4} a_w^4 c_q^4 + \alpha_n^3 \frac{1 + r_{p/q}^6}{64\sigma_w^6} a_w^6 c_q^6 + o(c_q^6) \end{aligned} \quad (24)$$

Taylor's theorem with remainder implies

$$H^2(P_0^n, P_1^n) \leq 1 - \left(1 - \alpha_n^2 \frac{1 + r_{p/q}^4}{32\sigma_w^4} a_w^4 c_q^4 \right)^{n_p}. \quad (25)$$

We seek to bound α_n to ensure covertness. Using covertness requirement δ and (12) implies

$$\delta \geq \sqrt{\frac{1}{2} \left(1 - \left(1 - \alpha_n^2 \frac{1 + r_{p/q}^4}{32\sigma_w^4} a_w^4 c_q^4 \right)^{n_p} \right)} \quad (26)$$

Rearranging yields

$$\alpha_n \leq \frac{4\sigma_w^2}{a_w^2 c_q^2} \sqrt{\frac{2(1 - (1 - 2\delta^2)^{1/n_p})}{1 + r_{p/q}^4}}. \quad (27)$$

Now, we substitute $1/n_p \rightarrow x^2$ and Taylor expand the right-hand side of (27) with respect to $x = 0$ as

$$\begin{aligned} & \frac{4\sigma_w^2}{a_w^2 c_q^2} \sqrt{\frac{2(1 - (1 - 2\delta^2)x^2)}{1 + r_{p/q}^4}} \\ &= \frac{4\sigma_w^2}{a_w^2 c_q^2} \sqrt{\frac{2 \log\left(\frac{1}{1-2\delta^2}\right)}{1 + r_{p/q}^4}} x \\ & - \frac{\sigma_w^2}{a_w^2 c_q^2} \sqrt{\frac{2 \log\left(\frac{1}{1-2\delta^2}\right)}{1 + r_{p/q}^4}} \log\left(\frac{1}{1-2\delta^2}\right) x^3 + o(x^3). \end{aligned} \quad (28)$$

Then, for n_p large enough, Taylor's theorem with remainder and reverting the substitution yields the expression in (13).

APPENDIX II PHASE ESTIMATION

In each pilot segment of the pulse, Bob receives the complex-valued vector

$$\vec{y}_p = a_b \vec{c}_p e^{j\theta_b} + \vec{z}_p^{(b)}, \quad (29)$$

where $\vec{z}_p^{(b)} \in \mathbb{C}^{n_s^{(p)}}$ is circularly-symmetric complex-valued AWGN afflicting the pilot segment. Applying the pilot-pulse-shape filter yields:

$$\langle \vec{c}_p, \vec{y}_p \rangle = a_b e^{j\theta_b} \|\vec{c}_p\|^2 + \langle \vec{c}_p, \vec{z}_p^{(b)} \rangle. \quad (30)$$

The expected values of the in-phase and quadrature (IQ) components $p_I \triangleq \Re(\langle \vec{c}_p, \vec{y}_p \rangle)$ and $p_Q \triangleq \Im(\langle \vec{c}_p, \vec{y}_p \rangle)$ are:

$$\mathbb{E}[\Re(\langle \vec{c}_p, \vec{y}_p \rangle)] = \mathbb{E}[p_I] = a_b \|\vec{c}_p\|^2 \cos(\theta_b) \quad (31)$$

$$\mathbb{E}[\Im(\langle \vec{c}_p, \vec{y}_p \rangle)] = \mathbb{E}[p_Q] = a_b \|\vec{c}_p\|^2 \sin(\theta_b), \quad (32)$$

since AWGN is circularly-symmetric and has zero mean. The estimate of phase θ_b is then $\hat{\theta}_b = \tan^{-1} \frac{p_I}{p_Q}$. As $n_s^{(p)}$ increases, p_I and p_Q converge to their expected values, yielding a more accurate estimate of phase. Here, $n_s^{(p)} = 26$ suffices.

APPENDIX III

DERIVATION OF OPTIMAL DETECTOR TEST STATISTIC

As in Appendix I, we substitute $\vec{c}_q \rightarrow c_q \vec{b}_q$ and $\vec{c}_p \rightarrow c_q r_{p/q} \vec{b}_p$ in the expression for L_i in (14) and Taylor expand it about $c_q = 0$:

$$\begin{aligned} L_i &= \frac{\alpha_n}{4\sigma_w^4} \left(r_{p/q}^2 \left(|\langle \vec{b}_p, \vec{p}_i \rangle|^2 - 2\sigma_w^2 \|\vec{b}_p\|^2 \right) \right. \\ & \quad \left. + |\langle \vec{b}_q, \vec{q}_i \rangle|^2 - 2\sigma_w^2 \|\vec{b}_q\|^2 \right) c_q^2 + o(c_q^2). \end{aligned} \quad (33)$$

Thus, for c_q sufficiently small, the i^{th} pulse-slot component $S_i^{(\text{opt})}$ of Willie's sufficient statistic is in (15).

APPENDIX IV

WILLIE'S DETECTORS' ERRORS

A. Analysis

Here, we derive bounds for the probability of error attainable by the optimal detector and radiometer, described in Section II-E. We use the Berry-Esseen theorem and assume non-informative priors. Both test statistics $S^{(\text{opt})}(\vec{w})$ and $S^{(\text{rad})}(\vec{w})$ have the form $S = \sum_{i=1}^{n_p} S_i$, where (S_i) is a sequence of realizations of n_p i.i.d. random variables. Let us standardize this sum using H_0 parameters:

$$S_{n_p} = \frac{S - n_p \mu_0}{\sigma_0 \sqrt{n_p}}, \quad (34)$$

where μ_0 and σ_0^2 are the mean and variance of S_i under H_0 . Similarly, let μ_1 and σ_1^2 be the mean and variance of S_i under H_1 , noting that they may depend on n_p . We provide the necessary moments of S_i under H_0 and H_1 for both optimal detector and radiometer in Appendix V.

Let $F_{n_p, h}(x)$ be the cumulative distribution function (c.d.f.) of the random variable statically describing S_{n_p} under H_h , $h \in \{0, 1\}$. By the Berry-Esseen theorem [71, Ch. XVI.5],

$$\sup_x |F_{n_p, k}(x) - \Phi(x)| \leq B_{n_p, k} \triangleq \frac{C \rho_k}{\sigma_k^3 \sqrt{n_p}}, \quad (35)$$

where ρ_k and σ_k are the absolute third central moment and the standard deviation of S_i under H_k , $\Phi(x)$ is the c.d.f. of standard Gaussian distribution $\mathcal{N}(0, 1)$, and $C < 0.4748$ is the Berry-Esseen constant. Willie decides between

H_0 and H_1 by comparing S_{n_p} to a threshold τ , per Section II-E. The probability of error given τ is $p_e^{(w)}(\tau) = \frac{1}{2} (P(S_{n_p} > \tau|H_0) + P(S_{n_p} \leq \tau|H_1))$. Applying (35), we have $P(S_{n_p} > \tau|H_0) = Q(\tau) + \epsilon_{n_p,0}$, where the approximation error $\epsilon_{n_p,0} \in [-B_{n_p,0}, B_{n_p,0}]$ and $Q(x) \triangleq \frac{1}{\sqrt{2\pi}} \int_x^\infty e^{-t^2/2} dt$ is the Gaussian error function. Under H_1 , we transform the event $S_n \leq \tau$ to the standardized frame of H_1 . Defining the effective argument $z(\tau) \triangleq \frac{\tau\sigma_0 - \sqrt{n_p}\Delta\mu}{\sigma_1}$, where $\Delta\mu = \mu_1 - \mu_0$, we have $P(S_{n_p} \leq \tau|H_1) = Q(-z(\tau)) + \epsilon_{n_p,1}$, where $\epsilon_{n_p,1} \in [-B_{n_p,1}, B_{n_p,1}]$. Thus, $p_e^{(w)}(\tau) = \frac{1}{2} (Q(\tau) + Q(-z(\tau))) + \frac{\epsilon_{n_p,0} + \epsilon_{n_p,1}}{2}$. The sum of Q -functions is minimized by symmetric arguments: $\tau = -z(\tau) = \frac{\sqrt{n_p}\Delta\mu}{\sigma_0 + \sigma_1}$. Thus, the minimum error probability achievable by both the optimum detector and the radiometer is:

$$p_{e,\text{det}}^{(w)} = Q\left(\frac{\sqrt{n_p}\Delta\mu}{\sigma_0 + \sigma_1}\right) + \frac{\epsilon_{n_p,0} + \epsilon_{n_p,1}}{2}, \quad (36)$$

with the distinction arising from the expressions for the moments being different for the detectors.

B. Discussion

When Alice follows the SRL, for both detectors, per Appendix V, $\Delta\mu \propto \frac{1}{\sqrt{n_p}}$ and $\sigma_1 \rightarrow \sigma_0$ as $n_p \rightarrow \infty$. Thus, $p_{e,\text{det}}^{(w)}$ converges to a constant, meaning neither detector is effective. On the other hand, when Alice does not follow the SRL, $p_{e,\text{det}}^{(w)} \rightarrow 0$ as $n_p \rightarrow \infty$, since $\sigma_0 + \sigma_1$ are upper-bounded by a constant, while $\sqrt{n_p}\Delta\mu$ is unbounded and $\epsilon_{n_p,0}, \epsilon_{n_p,1} \rightarrow 0$. This is borne out in our experiments.

Furthermore, since $p_{e,\text{det}}^{(w)}$ converges to $p_e^{(w)}$ in (10) for optimal detector as $n_p \rightarrow \infty$, Taylor series expansion of (36) around $\alpha_n = 0$ yields (16), which translates into $\approx 25\%$ improvement in α_n for $\delta = 0.07$ used here.

APPENDIX V MOMENTS OF WILLIE'S DETECTORS' SUFFICIENT STATISTICS

To analyze the error probability, we require the mean, variance, and upper bounds on the third absolute central moment of $S_i^{(\text{opt})}$ and $S_i^{(\text{rad})}$ under both hypotheses.

A. Optimal Detector

Under H_0 , observations follow complex Gaussian distributions $\vec{w}_i = (\vec{p}_i, \vec{q}_i) \sim \mathcal{CN}(\vec{0}, 2\sigma_w^2 \mathbf{I}_{n_s})$. Consequently, $S_i^{(\text{opt})}$ is a sum of two independent exponential random variables. The mean μ_0 and variance σ_0^2 are

$$\mu_0 = 2\sigma_w^2 (\|\vec{c}_p\|^2 + \|\vec{c}_q\|^2), \quad (37)$$

$$\sigma_0^2 = 4\sigma_w^4 (\|\vec{c}_p\|^4 + \|\vec{c}_q\|^4). \quad (38)$$

The Berry-Esseen bound relies on the third absolute central moment $\rho_0 = \mathbb{E}[|S_i - \mu_0|^3]$. We write $S_i - \mu_0 = (X - \mu_x) + (Y - \mu_y)$, where X and Y are independent exponential variables corresponding to the pilot and QPSK projections. Using the Minkowski inequality for the L_3 norm

$$\rho_0 = \|(X - \mu_x) + (Y - \mu_y)\|_3^3 \quad (39)$$

$$\leq (\|X - \mu_x\|_3 + \|Y - \mu_y\|_3)^3. \quad (40)$$

For an exponential variable X , $\|X - \mu_x\|_3 = \mu_x(12/e - 2)^{1/3}$. Substituting this yields an upper bound for ρ_0

$$\rho_0 \leq \left(\frac{12}{e} - 2\right) (\mu_x + \mu_y)^3 = \left(\frac{12}{e} - 2\right) \mu_0^3 \approx 2.415\mu_0^3. \quad (41)$$

Under H_1 , Willie receives a statistical mixture: with probability $1 - \alpha_n$, the slot contains only noise ($t = 0$), and with probability α_n , it contains signal ($t = 1$). The conditional mean given $t = 1$ is shifted by the signal energy $\Delta P = a_w^2 (\|\vec{c}_p\|^4 + \|\vec{c}_q\|^4)$

$$\mu_P = \mathbb{E}[S_i|t = 1] = \mu_0 + \Delta P. \quad (42)$$

The unconditional mean under H_1 is $\mu_1 = \mu_0 + \alpha_n(\mu_P - \mu_0) = \mu_0 + \alpha_n\Delta P$. Note that the difference in means is given by $\Delta\mu = \alpha_n\Delta P$.

The conditional variance given $t = 1$ involves non-central terms

$$\sigma_P^2 = \text{Var}[S_i|t = 1] = \sigma_0^2 + 4\sigma_w^2 a_w^2 (\|\vec{c}_p\|^6 + \|\vec{c}_q\|^6). \quad (43)$$

Using the law of total variance, the unconditional variance σ_1^2 is

$$\sigma_1^2 = \sigma_0^2 + \alpha_n(\sigma_P^2 - \sigma_0^2) + \alpha_n(1 - \alpha_n)(\Delta P)^2. \quad (44)$$

Analytically evaluating the third absolute central moment ρ_1 for the mixture distribution is intractable due to the absolute value function. Instead, we bound ρ_1 using the fourth central moment $\mu_{4,1}$ via Lyapunov's inequality $\rho_1 \leq (\mu_{4,1})^{3/4}$. The fourth central moment is derived algebraically from the raw moments. Let $m_k^{(0)} = \mathbb{E}[S_i^k|t = 0]$ and $m_k^{(1)} = \mathbb{E}[S_i^k|t = 1]$. The mixture raw moments are

$$\mathbb{E}[S_i^k] = (1 - \alpha_n)m_k^{(0)} + \alpha_n m_k^{(1)}. \quad (45)$$

From these, $\mu_{4,1}$ is obtained via the expansion

$$\mu_{4,1} = \mathbb{E}[S_i^4] - 4\mu_1\mathbb{E}[S_i^3] + 6\mu_1^2\mathbb{E}[S_i^2] - 3\mu_1^4 \quad (46)$$

and raw moments [72, Eq. following (29.31)]

$$m_k^{(1)} = \sum_{j=0}^k \binom{k}{j} \left[j! \beta_p^j L_j \left(-\frac{\lambda_p}{\beta_p} \right) \right] \times \left[(k-j)! \beta_q^{k-j} L_{k-j} \left(-\frac{\lambda_q}{\beta_q} \right) \right], \quad (48)$$

where $L_k(u)$ are Laguerre polynomials and $\beta_p = 2\sigma_w^2 \|\vec{c}_p\|^2$ and $\lambda_p = a_w^2 \|\vec{c}_p\|^4$ denote the noise power and signal energy for the pilot (similarly $\beta_q = 2\sigma_w^2 \|\vec{c}_q\|^2$, $\lambda_q = a_w^2 \|\vec{c}_q\|^4$ for QPSK).

B. Power Detector

Under H_0 , $\vec{w}_i \sim \mathcal{CN}(\vec{0}, 2\sigma_w^2 \mathbf{I}_{n_s})$. Consequently, $S_i^{(\text{rad})} = \|\vec{w}_i\|^2$ is a scaled central χ^2 random variable with $2n_s$ degrees of freedom and scaling factor σ_w^2 . The mean and variance are

$$\mu_0 = 2n_s\sigma_w^2, \quad (49)$$

$$\sigma_0^2 = 4n_s\sigma_w^4. \quad (50)$$

We again bound the third absolute central moment ρ_0 via Lyapunov's inequality $\rho_0 \leq (\mu_{4,0})^{3/4}$. The fourth central moment is given by

$$\mu_{4,0} = 48n_s\sigma_w^8(n_s + 2). \quad (51)$$

Under H_1 , the detector statistic is drawn from a mixture distribution. Conditioned on signal presence ($t = 1$), $S_i^{(\text{rad})}$ follows a scaled non-central χ^2 distribution with $2n_s$ degrees of freedom and non-centrality parameter $\lambda = \frac{\Delta P}{\sigma_w^2}$, with $\Delta P = a_w^2(\|\vec{c}_p\|^2 + \|\vec{c}_q\|^2)$. The conditional mean is then $\mu_P = \mu_0 + \Delta P$, and the unconditional mean is given by

$$\mu_1 = \mu_0 + \alpha_n \Delta P. \quad (52)$$

The conditional variance is $\sigma_P^2 = \sigma_0^2 + 4\sigma_w^2 \Delta P$. Applying the law of total variance, we obtain

$$\sigma_1^2 = \sigma_0^2 + \alpha_n(\sigma_P^2 - \sigma_0^2) + \alpha_n(1 - \alpha_n)\Delta P^2 \quad (53)$$

$$= \sigma_0^2 + 4\alpha_n\sigma_w^2\Delta P + \alpha_n(1 - \alpha_n)\Delta P^2. \quad (54)$$

We find the fourth central moment $\mu_{4,1}$ by expanding the moments of the mixture distribution. Let $\Delta\mu = \mu_1 - \mu_0 = \alpha_n\Delta P$ and $\Delta\mu' = \mu_P - \mu_1$. Now, we have

$$\begin{aligned} \mu_{4,1} &= (1 - \alpha_n)\mathbb{E}\left[\left(S_i^{(\text{rad})} - \mu_0 - \Delta\mu\right)^4 \middle| t = 0\right] \\ &\quad + \alpha_n\mathbb{E}\left[\left(S_i^{(\text{rad})} - \mu_P + \Delta\mu'\right)^4 \middle| t = 1\right]. \end{aligned} \quad (55)$$

Expanding the centered moments, the linear terms disappear, leaving

$$\begin{aligned} \mu_{4,1} &= (1 - \alpha_n)\left[\mu_{4,0} - 4\Delta\mu\mu_{3,0} + 6(\Delta\mu)^2\sigma_0^2 + (\Delta\mu)^4\right] \\ &\quad + \alpha_n\left[\mu_{4,P} + 4\Delta\mu'\mu_{3,P} + 6(\Delta\mu')^2\sigma_P^2 + (\Delta\mu')^4\right]. \end{aligned} \quad (56)$$

The third central moment for $t = 0$ is $\mu_{3,0} = 16n_s\sigma_w^6$. For $t = 1$, the moments are given by the cumulants of the scaled non-central χ^2 distribution [72, Ch. 29] as

$$\mu_{3,P} = 8\sigma_w^6\left(2n_s + 3\frac{\Delta P}{\sigma_w^2}\right) \quad (57)$$

$$\mu_{4,P} = 48\sigma_w^8\left(2n_s + 4\frac{\Delta P}{\sigma_w^2}\right) + 3\sigma_P^4. \quad (58)$$

APPENDIX VI

ESTIMATION OF WILLIE'S CHANNEL PARAMETERS

We need to estimate Willie's channel parameters from his observation and knowledge of \vec{c}_p and \vec{c}_q . An empty pulse slot received by Willie contains only noise:

$$\vec{w}_p(0) = \vec{z}^{(w)}, \quad (59)$$

The expectation of its squared magnitude is:

$$\mathbb{E}[\langle \vec{w}_p(0), \vec{w}_p(0) \rangle] = \mathbb{E}[\langle \vec{z}^{(w)}, \vec{z}^{(w)} \rangle] = 2n_s\sigma_w^2. \quad (60)$$

Thus, averaging over many instances of empty pulse slots and dividing by a known constant $2n_s$ yields an estimate $\hat{\sigma}_w^2$ of σ_w^2 . This can be used to estimate μ_0 and σ_0^2 for both the optimal detector and the radiometer, as per Appendix V. Similarly, one can estimate a_w^2 from the pulse slots used for transmission.

Now, denote the test statistic for either detector under hypothesis H_h , $h \in \{0, 1\}$ by $S^{(h)}$. After normalizing, $\frac{S^{(h)}}{n_p} \rightarrow \mathbb{E}\left[S_i^{(h)}\right]$ by Law of Large Numbers. Arithmetic and estimate of σ_w^2 yield the quantities we need to calculate the threshold.

REFERENCES

- [1] B. A. Bash, D. Goeckel, and D. Towsley, "Square root law for communication with low probability of detection on AWGN channels," in *Proc. IEEE Int. Symp. Inform. Theory (ISIT)*, Cambridge, MA, Jul. 2012.
- [2] —, "Limits of reliable communication with low probability of detection on AWGN channels," *IEEE J. Select. Areas Commun.*, vol. 31, no. 9, pp. 1921–1930, 2013.
- [3] B. A. Bash, D. Goeckel, S. Guha, and D. Towsley, "Hiding information in noise: Fundamental limits of covert wireless communication," *IEEE Commun. Mag.*, vol. 53, no. 12, 2015.
- [4] X. Chen, J. An, Z. Xiong, C. Xing, N. Zhao, F. R. Yu, and A. Nallanathan, "Covert communications: A comprehensive survey," *IEEE Commun. Surv. Tutor.*, vol. 25, no. 2, pp. 1173–1198, 2023.
- [5] A. J. Menezes, S. A. Vanstone, and P. C. V. Oorschot, *Handbook of Applied Cryptography*. Boca Raton, FL, USA: CRC Press, Inc., 1996.
- [6] M. R. Bloch and J. Barros, *Physical-Layer Security*. Cambridge University Press, 2011.
- [7] M. K. Simon, J. K. Omura, R. A. Scholtz, and B. K. Levitt, *Spread Spectrum Communications Handbook*. McGraw-Hill, 1994.
- [8] T. M. Cover and J. A. Thomas, *Elements of Information Theory*, 2nd ed. John Wiley & Sons, Hoboken, NJ, 2002.
- [9] M. R. Bloch, "Covert communication over noisy channels: A resolvability perspective," *IEEE Trans. Inf. Theory*, vol. 62, no. 5, pp. 2334–2354, May 2016.
- [10] L. Wang, G. W. Wornell, and L. Zheng, "Fundamental limits of communication with low probability of detection," *IEEE Trans. Inf. Theory*, vol. 62, no. 6, pp. 3493–3503, Jun. 2016.
- [11] M. Tahmasbi and M. R. Bloch, "First and second order asymptotics in covert communication," *IEEE Trans. Inf. Theory*, vol. 65, no. 4, pp. 2190–2212, Apr. 2019.
- [12] Y. Xinchun, S. Wei, S.-L. Huang, and X. P. Zhang, "On the second order asymptotics of covert communications over awgn channels," in *Proc. IEEE Int. Conf. Commun. (ICC)*, 2024, pp. 1479–1484.
- [13] K. S. K. Arumugam and M. R. Bloch, "Covert communication over broadcast channels," in *Proc. Inform. Theory Workshop (ITW)*, Nov. 2017, pp. 299–303.
- [14] J. Hu, S. Yan, X. Zhou, F. Shu, and J. Wang, "Covert communication in wireless relay networks," arXiv:1704.04946 [cs.IT], Apr. 2017.
- [15] J. Hu, S. Yan, X. Zhou, F. Shu, J. Li, and J. Wang, "Covert communication achieved by a greedy relay in wireless networks," *IEEE Trans. Wireless Commun.*, vol. 17, no. 7, pp. 4766–4779, 2018.
- [16] K. S. K. Arumugam and M. R. Bloch, "Covert communication over a k-user multiple access channel," *IEEE Trans. Inf. Theory*, vol. 65, no. 11, pp. 7020–7044, Nov. 2019.
- [17] V. Y. F. Tan and S. Lee, "Time-division is optimal for covert communication over some broadcast channels," *IEEE Trans. Inf. Forensics Security*, vol. 14, no. 5, pp. 1377–1389, May 2019.
- [18] A. Sheikholeslami, M. Ghaderi, D. Towsley, B. A. Bash, S. Guha, and D. Goeckel, "Multi-hop routing in covert wireless networks," *IEEE Trans. Wireless Commun.*, vol. 17, no. 6, pp. 3656–3669, Jun. 2018.
- [19] R. Soltani, D. Goeckel, D. Towsley, B. A. Bash, and S. Guha, "Covert wireless communication with artificial noise generation," *IEEE Trans. Wireless Commun.*, vol. 17, no. 11, pp. 7252–7267, Nov. 2018.
- [20] T.-X. Zheng, H.-M. Wang, D. W. K. Ng, and J. Yuan, "Multi-antenna covert communications in random wireless networks," *IEEE Trans. Wireless Commun.*, vol. 18, no. 3, pp. 1974–1987, 2019.
- [21] Z. Liu, J. Liu, Y. Zeng, and J. Ma, "Covert wireless communication in iot network: From awgn channel to thz band," *IEEE Internet Things J.*, vol. 7, no. 4, pp. 3378–3388, 2020.
- [22] K.-H. Cho, S.-H. Lee, and V. Y. F. Tan, "Throughput scaling of covert communication over wireless adhoc networks," *IEEE Trans. Inf. Theory*, vol. 66, no. 12, pp. 7684–7701, 2020.
- [23] N. Q. Hieu, D. T. Hoang, D. Niyato, D. N. Nguyen, D. I. Kim, and A. Jamalipour, "Joint power allocation and rate control for rate splitting multiple access networks with covert communications," *IEEE Trans. Commun.*, vol. 71, no. 4, pp. 2274–2287, 2023.

- [24] J. Kong, F. T. Dagefu, and T. J. Moore, "Covert routing in heterogeneous networks," *IEEE Trans. Inf. Forensics Security*, vol. 19, pp. 7047–7059, 2024.
- [25] S. Zhao, J. Liu, Y. Shen, X. Jiang, T. Taleb, and N. Shiratori, "On the impact of warden collusion on covert communication in wireless networks," *IEEE Trans. Inf. Forensics Security*, vol. 20, pp. 2297–2312, 2025.
- [26] B. A. Bash, S. Guha, D. Goeckel, and D. Towsley, "Quantum Noise Limited Communication with Low Probability of Detection," in *Proc. IEEE Int. Symp. Inform. Theory (ISIT)*, Istanbul, Turkey, Jul. 2013.
- [27] B. A. Bash, A. H. Gheorghie, M. Patel, J. L. Habif, D. Goeckel, D. Towsley, and S. Guha, "Quantum-secure covert communication on bosonic channels," *Nat. Commun.*, vol. 6, Oct. 2015.
- [28] A. Sheikholeslami, B. A. Bash, D. Towsley, D. Goeckel, and S. Guha, "Covert communication over classical-quantum channels," in *Proc. IEEE Int. Symp. Inform. Theory (ISIT)*, Barcelona, Spain, Jul. 2016.
- [29] M. S. Bullock, C. N. Gagatsos, S. Guha, and B. A. Bash, "Fundamental limits of quantum-secure covert communication over bosonic channels," *IEEE J. Sel. Areas Commun.*, vol. 38, no. 3, pp. 471–482, Mar. 2020.
- [30] C. N. Gagatsos, M. S. Bullock, and B. A. Bash, "Covert capacity of bosonic channels," *IEEE J. Sel. Areas Inf. Theory*, vol. 1, pp. 555–567, 2020.
- [31] M. Tahmasbi and M. R. Bloch, "Toward undetectable quantum key distribution over bosonic channels," arXiv:1904.12363 [cs.IT], 2019.
- [32] —, "Toward undetectable quantum key distribution over bosonic channels," *IEEE J. Sel. Areas Inf. Theory*, vol. 1, no. 2, pp. 585–598, 2020.
- [33] E. J. Anderson, S. Guha, and B. A. Bash, "Fundamental limits of bosonic broadcast channels," in *Proc. IEEE Int. Symp. Inform. Theory (ISIT)*, virtual, Jul. 2021.
- [34] S.-Y. Wang, T. Erdođan, and M. Bloch, "Towards a characterization of the covert capacity of bosonic channels under trace distance," in *Proc. IEEE Int. Symp. Inf. Theory (ISIT)*. IEEE Press, 2022, pp. 318–323.
- [35] E. J. D. Anderson, C. K. Eyre, I. M. Dailey, F. Rozpędek, and B. A. Bash, "Square root law for covert quantum communication over optical channels," in *Proc. IEEE Int. Conf. Quantum Comput. Eng. (QCE)*, Montréal, QC, Canada, 2024.
- [36] M. S. Bullock, A. Sheikholeslami, M. Tahmasbi, R. C. Macdonald, S. Guha, and B. A. Bash, "Fundamental limits of covert communication over classical-quantum channels," *IEEE Trans. Inf. Theory*, vol. 71, pp. 2741–2762, Apr. 2025.
- [37] E. Zlotnick, B. A. Bash, and U. Pereg, "Entanglement-assisted covert communication via qubit depolarizing channels," *IEEE Trans. Inf. Theory*, vol. 71, no. 5, pp. 3693–3706, 2025.
- [38] X. Jiang, X. Chen, J. Tang, N. Zhao, X. Y. Zhang, D. Niyato, and K.-K. Wong, "Covert communication in uav-assisted air-ground networks," *IEEE Wireless Commun.*, vol. 28, no. 4, pp. 190–197, 2021.
- [39] X. Chen, N. Zhang, J. Tang, M. Liu, N. Zhao, and D. Niyato, "Uav-aided covert communication with a multi-antenna jammer," *IEEE Trans. Veh. Technol.*, vol. 70, no. 11, pp. 11 619–11 631, 2021.
- [40] C. Wang, X. Chen, J. An, Z. Xiong, C. Xing, N. Zhao, and D. Niyato, "Covert communication assisted by uav-irs," *IEEE Trans. Commun.*, vol. 71, no. 1, pp. 357–369, 2023.
- [41] W. Tian, J. Du, X. Ji, M. Du, G. Liu, and Z. Han, "Uav-enabled communication strategy against detection in covert communication with asymmetric information," *IEEE Trans. Wireless Commun.*, vol. 23, no. 7, pp. 6921–6937, 2024.
- [42] J. Xu, L. Bai, X. Xie, and L. Zhou, "Collaborative secret and covert communications for multi-user multi-antenna uplink uav systems: Design and optimization," *IEEE Trans. Wireless Commun.*, vol. 24, no. 7, pp. 6020–6035, 2025.
- [43] Z. Wu, K. Guo, C. Dong, M. Wu, S. Zhu, C. Li, and Q. Wu, "Covert communications for uav-assisted network: A comprehensive survey," *Chin. J. Aeronaut.*, p. 103750, 2025.
- [44] Z. Li, J. Shi, J. Si, L. Lv, L. Guan, B. Hao, Z. Tie, D. Wang, C. Xing, and T. Q. Quek, "Intelligent covert communication: Recent advances and future research trends," *Engineering*, vol. 44, pp. 101–111, 2025.
- [45] B. A. Bash, D. Goeckel, and D. Towsley, "LPD Communication when the Warden Does Not Know When," in *Proc. IEEE Int. Symp. Inform. Theory (ISIT)*, Honolulu, HI, Jul. 2014.
- [46] —, "Covert communication gains from adversary's ignorance of transmission time," *IEEE Transactions on Wireless Communications*, vol. 15, no. 12, pp. 8394–8405, Dec. 2016, Originally presented at ISIT 2014, Honolulu HI.
- [47] K. S. K. Arumugam and M. R. Bloch, "Keyless asynchronous covert communication," in *Proc. Inform. Theory Workshop (ITW)*, Sep. 2016.
- [48] T. V. Sobers, B. A. Bash, D. Goeckel, S. Guha, and D. Towsley, "Covert communication with the help of an uninformed jammer achieves positive rate," in *Asilomar Conf. Signals Syst. Comput.*, Pacific Grove, CA, USA, Nov. 2015, pp. 625–629.
- [49] T. V. Sobers, B. A. Bash, S. Guha, D. Towsley, and D. Goeckel, "Covert communication in the presence of an uninformed jammer," *IEEE Trans. Wireless Commun.*, vol. 16, no. 9, pp. 6193–6206, Sep. 2017.
- [50] T. Zheng, H. Wang, D. W. K. Ng, and J. Yuan, "Multi-antenna covert communications in random wireless networks," *IEEE Trans. Wireless Commun.*, vol. 18, no. 3, pp. 1974–1987, 2019.
- [51] T.-X. Zheng, Z. Yang, C. Wang, Z. Li, J. Yuan, and X. Guan, "Wireless covert communications aided by distributed cooperative jamming over slow fading channels," *IEEE Trans. Wireless Commun.*, vol. 20, no. 11, pp. 7026–7039, 2021.
- [52] A. Gillani, T. V. Sobers, D. Towsley, and D. Goeckel, "Covert communications under environmental uncertainty on a continuous-time channel," in *Proc. Asilomar Conf. Signals Syst. Comput.*, 2023, pp. 248–252.
- [53] Y. Liu, J. M. Arrazola, W.-Z. Liu, W. Zhang, I. W. Primaatmaja, H. Li, L. You, Z. Wang, Q. Zhang, and J.-W. Pan, "Experimental covert communication over metropolitan fibre optical links," *IEEE Wireless Commun.*, vol. 31, no. 4, pp. 76–80, 2024.
- [54] I. B. Djordjevic and I. A. Rojas, "Entanglement assisted LPI and covert communications with SLM-based beam steering over turbulent optical channels," *IEEE Access*, vol. 13, pp. 174 658–174 663, 2025.
- [55] —, "SLM steering-based covert communication over strong atmospheric turbulence channels," *Opt. Express*, vol. 33, no. 21, pp. 44 622–44 630, Oct. 2025.
- [56] D. Raychaudhuri, I. Seskar, M. Ott, S. Ganu, K. Ramachandran, H. Kremo, R. Siracusa, H. Liu, and M. Singh, "Overview of the ORBIT radio grid testbed for evaluation of next-generation wireless network protocols," in *IEEE Wireless Commun. Netw. Conf. (WCNC)*, vol. 3, 2005, pp. 1664–1669.
- [57] ORBIT Project, "Grid domain overview," [Online] Available: <https://www.orbit-lab.org/wiki/Hardware/bDomains/aGrid>, 2026, accessed: March 6, 2026.
- [58] S.-Y. Wang and M. R. Bloch, "Explicit design of provably covert channel codes," in *IEEE Int. Symp. Inf. Theory (ISIT)*, 2021, pp. 190–195.
- [59] D. Tse and P. Viswanath, *Fundamentals of Wireless Communication*. Cambridge University Press, 2005.
- [60] D. Slepian, "Prolate spheroidal wave functions, fourier analysis, and uncertainty — v: the discrete case," *The Bell System Technical Journal*, vol. 57, no. 5, pp. 1371–1430, 1978.
- [61] T. Richardson and R. Urbanke, *Modern Coding Theory*. Cambridge University Press, 2008.
- [62] E. Lehmann and J. Romano, *Testing Statistical Hypotheses*, 4th ed. Cham, Switzerland: Springer, 2022.
- [63] Ettus Research, "Octoclock and octoclock-g product overview," https://www.ettus.com/wp-content/uploads/2019/01/Octoclock_Spec_Sheet.pdf, Jan. 2019, accessed: March 6, 2026.
- [64] —, "UHD: USRP hardware driver," GitHub repository, 2025, [Online]. Available: <https://github.com/EttusResearch/uhd>. Accessed: March 6, 2026.
- [65] —, "USRP hardware driver and USRP manual," [Online]. Available: <https://files.ettus.com/manual/index.html>, version 4.9.0.0. Accessed: March 6, 2026.
- [66] Ettus Research, a National Instruments Company, "USRP™ X300/X310 Networked Series: Specification Sheet," [Online] Available: https://www.ettus.com/wp-content/uploads/2019/01/X300_X310_Spec_Sheet.pdf, Accessed: March 6, 2026, 2019.
- [67] B. Letham, B. Karrer, G. Ottoni, and E. Bakshy, "Ax: Adaptive experimentation platform, ver. 1.0.0," [Online] Available: <https://github.com/facebook/ax>, Accessed: March 6, 2026, 2025.
- [68] P. Hennig, M. A. Osborne, and H. P. Kersting, *Probabilistic Numerics: Computation as Machine Learning*. Cambridge University Press, 2022.
- [69] C. K. Williams and C. E. Rasmussen, *Gaussian processes for machine learning*. MIT press Cambridge, MA, 2006, vol. 2, no. 3.
- [70] N. R. Draper and H. Smith, *Applied Regression Analysis*. John Wiley & Sons, Inc., 1998.
- [71] W. Feller, *Introduction to Probability Theory and its Applications, Volume II*, 2nd ed. New York: John Wiley & Sons., 1971.
- [72] N. L. Johnson, S. Kotz, and N. Balakrishnan, *Continuous Univariate Distributions*, ser. Distributions in Statistics. New York: John Wiley & Sons, 1995, vol. 2.